Hydration of Tricalcium Silicate

Andrew Chiu

Supervisor: Prof. Ian Robinson

31st March 2016

PHASM201: Physics Project

University College London

Department of Physics and Astronomy

Abstract

The hydration of Tricalcium Silicate (C3S) has been studied via X-ray powder diffraction for two different grain sizes and the Williamson-Hall method used to extract trends in lattice micro-strain and average crystallite sizes, over a 28 day measurement period. TXM images have been obtained for a C3S grain hydrated at 1:2 w/s ratio, and the internal pore structure examined, for 5 days and 28 days post hydration.

XRPD measurements imply a positive relation between smaller grain sizes and higher reaction rate. Greater quantities of portlandite were formed from the smaller grains compared to bigger grains. Lattice strain and crystallite size were proportional for the small grains throughout the full 28 days, and between 1-28 days for the big particles.

Careful study of the TXM images between 5 days and 28 days post hydration show no change in pore structure or grain size, implying the hydration rate within this time frame is either too slow to observe, or has terminated due to a water loss or otherwise.

Acknowledgements

I would like to express my sincerest gratitude to Professor Ian Robinson for his continued guidance and approachability throughout the year who has made this project all the more engaging, and I would also like to thank Bo Chen for his constant aid and advice with data collection and sample preparation.

Contents

Glossary

Cement Chemistry Notation (CCN)

C	CaO
H	H_2O
S	SiO_2
A	Al_2O_3
F	Fe_2O_3
C3S	$3CaO \cdot SiO_2$
C2S	$2CaO \cdot SiO_2$
C3A	$3CaO \cdot Al_2O_3$
$4\ CaO \bullet Al_2O_3 \bullet Fe_2O_3$	$4CaO \cdot Al_2O_3 \cdot Fe_2O_3$

1. Introduction

This project was set out to investigate the change in microstructural properties of Tricalcium silicate upon hydration via x-ray powder diffraction methods. XRPD provides a non-intrusive method of tracking changes in crystalline phases during hydration. In this experiment, the change of crystallite size and lattice strain within a 28day period will be studied for two differing particle sizes, with the prospect of gaining

2. Cement Hydration

2.1 Structure and Hydration of Tricalcium Silicate

Portland cement, the most commonly used cement mixture is composed of ~50-90% Tricalcium silicate (C3S), making it arguably the most important hydraulic phase for study. It reacts reletively quickly with water, reaching 70% completion within 28days. A secondary silicate phase, C2S comprises 15-30% of the mixture. It reacts noticable slower than C3S, thus has more relevance to the strength development post 28 days. The other hydraulic phase, C3A makes up ~5-10% of the mixture, and reacts the fastest of all phases releasing significant heat within the initial moment of hydration. It is therefore known for its 'flash-setting' properties, causing potentiall undesirable hardening of the cement, thus a gypsum is added to inhibit the reaction [1]. There is also a ferrite phase, C4AF which hydrates rapidly, but contributes little to the overall strength development in cement. It is used for lower kiln temperatures during the manufactering stage.

The reaction of C3S with water is as follows:

$$C_3S + (3 - x + n)H \rightarrow C_xSH_n + (3 - x)CH \tag{2.1}$$

Where x is the water to cement ratio.

The strength development of C3S is believed to be due to the formation of a calcium-sliicate-hydrate (CSH) gel phase, which is variable in composition depending on the amount of water present [2]. The other hydration product, calcium hydroxide (CH), or portlandite in its mineral form, crystallises when the solution is saturated with CH. It is important for indicating the end of a hydration stage as it crystallises out of the solution.

C3S has seven polymorpic phases which exist in the triclinic, monoclinic or rhombohedral form determined by the temperature during the sintering process of cement production. In industrial clinkers, the monoclinic phases are most abundant, however pure C3S is a triclinic structure [3].

The underlying hydration mechanism of C3S is a constantly evolving field, with no universally agreed upon mechanism set in stone. However, the rate of hydration is commonly characterised into 4 to 5 stages by plotting a calorimetry curve against time (fig. 1-1). The details of each stages are uncertain, especially within the initial reaction period which occurs within a short timespan.

The initial reaction period takes place within the first seconds, lasting several minutes typically. When C3S comes into contact with water, a rapid dissolution of ions from the surface takes place, C3S hydrolyses into Ca2+, OH- and H2SiO4 2-. This reaches maximum hydration rate when the concentration of calcium and silicate ions supersaturate the solution, where the hydration enters the next stage coined the induction period.

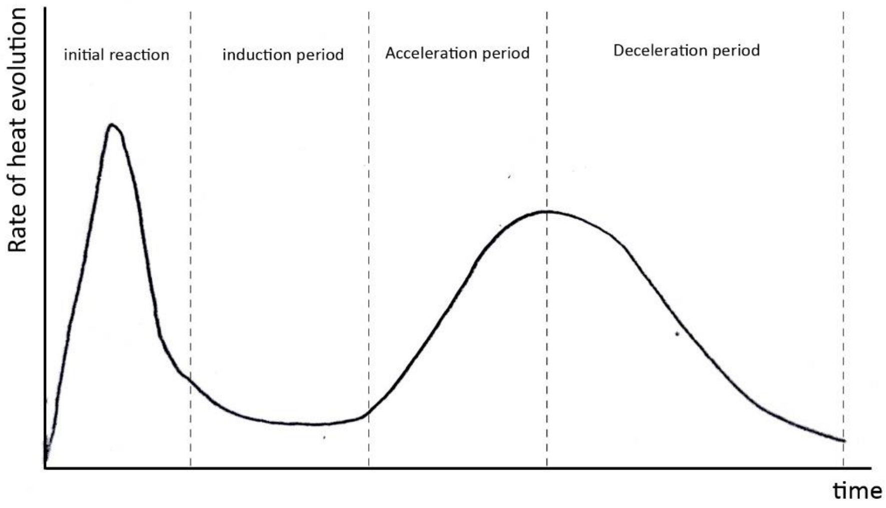

Figure 2-1: Rate of hydration vs time, typically using calorimetry.

The induction period is characterised by an interval of extremely limited progression, typically lasting several hours in length. There have been several theories which attempt to elucidate the mechanism with varying degrees of experimental data backing them up.

1. A CSH layer precipitates on surface of the C3S grains preventing dissolution of C3S. SEM measurements have shown that CSH forms a fibrous, 'needle' like structure on the grain surface [4], which leads to a decrease in concentation of silicate ions, as the concentration of CSH increases [5]. Reasons for termination include: CSH 'barrier' weakens due to age, diffusion of C3S ions through the barrier until critical saturation is reached, or CH reaches saturation and precipitates from the solution as portlandite.
2. Silicate ions poisons the CH nuclei preventing nucleation into crystals even when saturation of CH in solution is reached. This terminates when the dissolution of C3S and CSH formation slows down, and the solution reaches critical saturation of unpoisoned CH which precipitates are portlandite [6].

The end of the induction period and start of the acceleration period can be characterised by the precipitation of CH into portlandite. Precipitation of CH creates more space for other ions to fill, thus dissolution of C3S continues and the acceleration period begins. X-ray powder diffraction (XRPD) can see this as a new peak growth for portlandite; but CSH cannot be detected due to its amorphous nature.

Hydrated C3S consists of capillary pores formed from the dissolution of C3S. Pores begin on the surface as holes and penetrate deeper into the cement as hydration progresses. This may eventually form an interconnected network of pores, which are of significance in the transportation of the solution, which contains ions. The pores vary in size from nm to several microns [7], with small pores forming for smaller particle sizes. The presence of pores changes the density, and in turn the strength of the hardened cement. The w/c (water to cement) ratio required for the complete hydration of C3S is about 0.42 [1]

3. Theory behind experimental techniques

3.1 X-ray Powder Diffraction

The major advantage of using XRPD to characterize the phases and evolution of cement hydration is the ability to record data in a relatively continuous fashion (i.e. ~30-minute scan segments over 0-90°). One can record the diffraction patterns relatively quickly; so in this case, two hydrating samples of interest can be continuously interchanged one after the other. Of course we are limited to lab-based power sources, but synchrotron XRPD are able to obtain time resolutions within the minutes range [8].

Powder diffraction operates under the theory that within a powder sample, there are several crystals orientated over the course of a Θ-2Θ scan which will be in the correct orientation to satisfy Bragg's Law for coherent diffraction.

$$n\lambda = 2d\sin\theta \qquad (3.1)$$

Where λ is the wavelength of the x-ray, d is the interatomic spacing between lattice planes, and θ is the angle of diffraction.

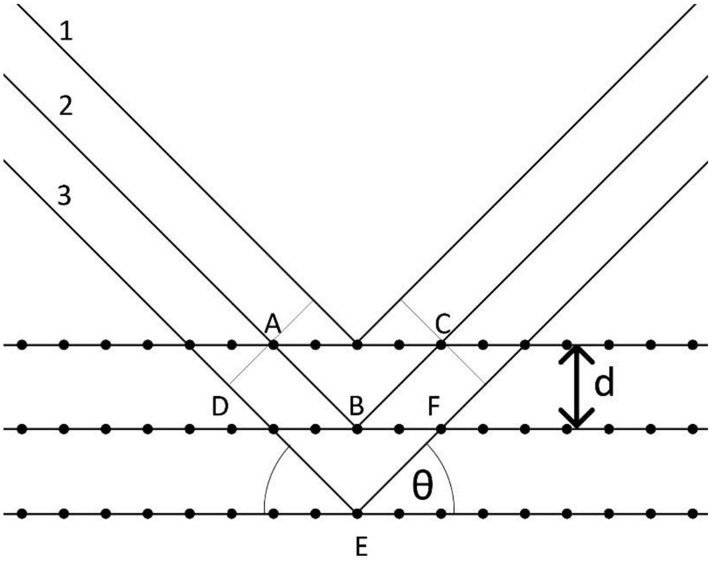

Figure 3-1: Bragg's Law. Figure adapted from [9] *and* [10].

See figure 1-1. For Bragg's law to be satisfied, beams 2 and 3 have a phase difference of ABC and DEF with respect to the beam 1, where ABC = λ and DEF = 2λ in length and nλ for subsequent planes [10]. The sum of these scattered waves from all the planes will interfere constructively resulting in an intense outgoing wave known as diffraction.

3.1.1 Structure determination

Diffracting planes within a crystal lattice are defined by labels known as Miller indices. In real space, the lattice vector is defined as:

$$R = n_1\boldsymbol{a_1} + n_2\boldsymbol{a_2} + n_3\boldsymbol{a_3}$$

Where $a_{1,2,3}$ are the lattice parameters (of the unit cell) defining the basis of the system.

In reciprocal space, the reciprocal lattice vector is defined as:

$$G_{hkl} = \boldsymbol{a_1}^*h + \boldsymbol{a_2}^*k + \boldsymbol{a_3}^*l \qquad (3.2)$$

$a_{1,2,3}{}^*$ are the reciprocal lattice vectors defined as

$$\boldsymbol{a_{1,2,3}}^* = \frac{2\pi(\boldsymbol{a_{2,3,1}} \times \boldsymbol{a_{3,1,2}})}{\boldsymbol{a_1}(\boldsymbol{a_2} \times \boldsymbol{a_3})}$$

G is defined as the reciprocal lattice vector perpendicular to a plane in real space. The lattice points closest to the origin are intercepted by lattice planes at (a1/h, a2/k, a3/l), where (hkl) define the miller indices of the planes separated by:

$$d_{hkl} = \frac{a}{\sqrt{h^2 + k^2 + l^2}} \qquad (3.3)$$

Therefore, the structure of a crystal can be identified from the Miller indices extracted as the spacing and angle of diffraction is already known from measurements.

Reference databases for different crystal compounds contained the spacing and intensity of diffraction patterns are used for this purpose of comparing known patterns with experimentally obtained ones.

3.1.2 Factors affecting peak shapes

In an ideal scenario, a powder sample would contain infinitely many grains all oriented in random directions to produce a high intensity peak, described by a Gaussian or Lorentzian function. In practice, the diffraction pattern from differing samples have often have features deviating from the idealised profile. Possible reasons will be discussed in this section.

Peak broadening is normally described by two parameters.

- FWHM (full-width at half maximum): Full width at half of the maximum height.

- Integral breadth, β: peak area/maximum intensity

At high 2θ angles, kα1 and kα2 peak splitting is more pronounced, where the kα2 is seen as a shoulder on the right of the kα1 peak. This is easily explained by Bragg's law:

$$\theta = \sin^{-1}\left(\frac{\lambda}{2d}\right)$$

For peaks at larger angles (small d), the splitting is more pronounced (table 3-1).

	d=1 Å	d=10 Å
λ (Cu-kα1)= 1.5406Å	2θ=50.38°	2θ=8.836°
λ (Cu-kα2)= 1.5443Å,	2θ=50.55°	2θ=8.857°

Table 3-1: kα1 kα2 splitting at higher peak positions.

In the case of pointy, or plate like structures for example, these grains may have a tendency to lie flat along the plane of the sample holder for example, enhancing and reducing the intensity of Bragg reflections as particular planes are exposed or hidden to the x-ray.

Amorphous structures will display broad low intensity humps as there exists in long range order (crystallinity) and only short range order like a glass. The range of d values and lack of Bragg planes for constructive interference results in a broad peak centred around the crystalline phase.

3.1.3 Detector Geometry

The most commonly used optical setup nowadays is the Bragg-Brentano geometry. The source, sample and detector all lie along the circumference of a focusing circle, where the source to sample, and detector to sample are an equal fixed distance. The source and detector arms both rotate at the same angular velocity where divergent beams diffract from the flat sample surface and are focused into the detector (fig. 3-1). The goniometer circle is centred around the sample where the detector traces along its circumference through an angle 2Θ.

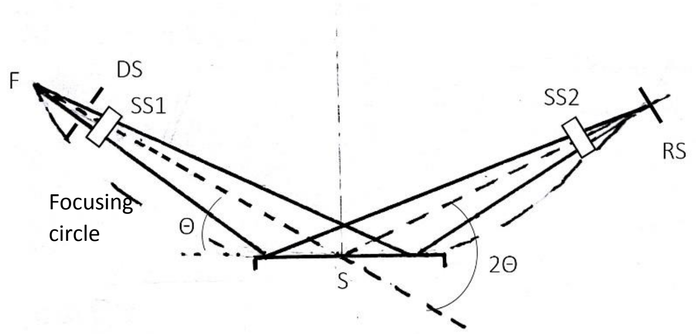

Figure 3-2: Bragg-Brentano geometry schematic diagram. DS=Diffraction slit, SS1/2 = Soller slits, RS= Receiving slit. Adapted from Jenkins et al [10].

An x-ray source at F emits a divergent beam which passes through a divergence slit (DS) before the soller slit (SS1), which both control the degree of divergence. DS controls how much of the sample is illuminated, whereas the soller slits are a series of metal sheets that collimate the beam, limiting horizontal divergence. Narrower soller slits may increase resolution, but decrease peak intensities. This may be useful where identifying overlapping peaks from different compounds is required [11].

The diffracted beam passes through a secondary collimator (SS2) limiting background noise, and continuing through a receiving slit which limits the beam width before reaching the detector. Increasing RS similarly increases peak intensity at expense of resolution [10].

The sample should ideally follow the curvature of the focusing circle, however this is highly unlikely for a flat sample holder which is more likely tangent to the circle. The consequence is the beam arriving at a slightly lower angle than the than the actual position of the receiving slit, shifting the peak intensity and broadening of the diffraction profile to a lower $2\ \Theta$. Adopting a smaller divergence slit would help at the loss of intensity [12].

3.2 Transmission X-ray Microscopy

Transmission X-ray microscopy works on largely the same principle as the well-established medical CT scan for imaging 2D slices within 3D bodies. Computed Tomography was introduced as a way to resolve the problem of blurring in Classical tomography where a reconstructed 2D image was blurred due to the overlap from several points of view of the 3D body for which the x-ray beam passes through [13]. Back projection is a technique which attempts to correct for this blurring.

3.2.1 Back Projection

Take fig. 3-4 representing the signal output acquired for a circular sample from three different views (although several views are used in practice, three are shown to explain). As expected, we see a large signal where absorption is highest. If we take each signal, 'smear' (back project) them and add each projection together, we begin to see a semblance to the original image at the overlap (fig. 3-5). Replicating for a large number of views (such as every 1°), the object is more discernible, but still surrounded by a 'halo': - A point of highest intensity with a radially decreasing intensity proportional to the reciprocal of the radius from the ROI (region of interest) (fig. 3-6).

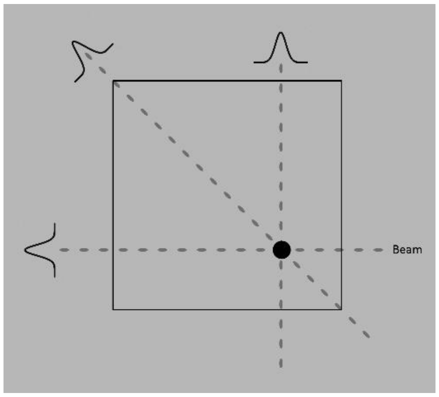

Figure 3-5:Object using three different views.

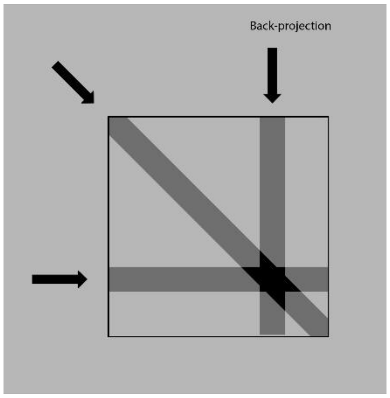

Figure 3-4: Signals back projected and added together using three views

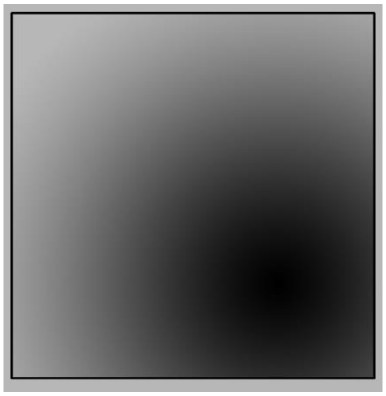

Figure 3-3:Final image: Process repeated using large number of views. Radial blur due to overlap of projections.

The original image $I(x, y)$ function (thought of as pixel intensity value from x-ray) of the scanned volume in Cartesian space can be related to the 1D projection function (acquired data) $g(\rho, \theta)$, via the Radon transformation [14]. Where ρ equals the perpendicular distance of the x-ray beam from the axis y' through the origin (see fig.3-6) and θ is the tilt of the projection plane (i.e the detectors orientation relative to the object).

$$g(\rho, \theta) = \int_{-\infty}^{\infty} \int_{-\infty}^{\infty} I(x, y) \delta(\rho = x cos\theta + y sin\theta)\, dxdy \tag{1}$$

The delta function is to ensure only the points lying along the beam at ρ are integrated.

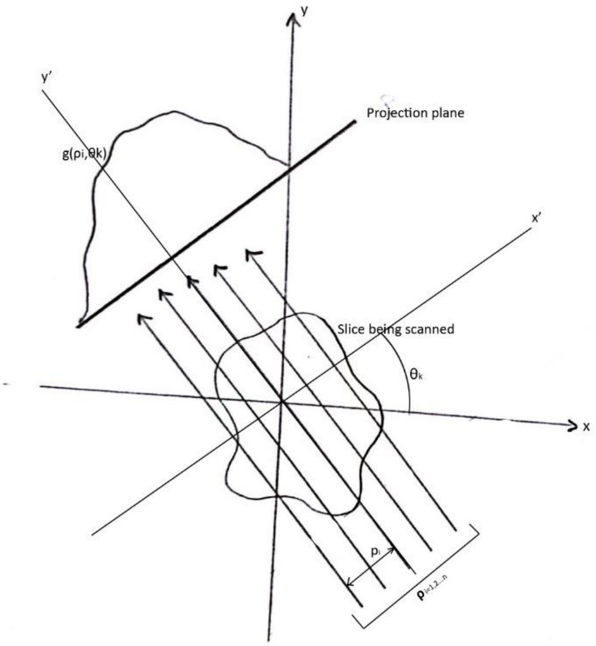

Figure 3-6- 2D image function I(x,y) related to 1D Projection function g(ρ, ϑ).

The back projection is completed by copying the value of $g(\rho i, \theta k)$ along its corresponding line ρ_i onto the image at (x, y), given by $f_\theta(x, y) = g(\rho i, \theta k)$.

$$\int_0^{\pi} f_\theta(x,y)\,d\theta \tag{2}$$

Integrating over 180° sums up all the back projections at (x, y) from taking projections at 0°-180°. [15]

3.2.2 Fourier-Slice Theorem

The Fourier transform of the projection function $g(\rho,\theta)$ in 1D can be related to the 2D Fourier transform of a slice from which the projection was obtained from [14].

$$G(\omega,\theta) = \int_{-\infty}^{\infty} g(\rho,\theta)e^{-i2\pi w\rho}d\rho \tag{3}$$

This is the 1D Fourier transform of the projection function w.r.t ρ at fixed θ, into frequency space ω.

Plugging in the Radon transform $g(\rho,\theta)$ and applying a change of variables $u = \omega\cos\theta\,, v = \omega\sin\theta$ to the exponential:

$$G(\omega,\theta) = \int_{-\infty}^{\infty} I(x,y)e^{-i2\pi(ux+vy)}dxdy \tag{4}$$

Notice how this is equal to the image function in (u, v) space.

$$G(\omega,\theta) = I(u,v) \tag{5}$$

Giving the Fourier transform of the image slice as desired, hence the actual object can be reconstructed.

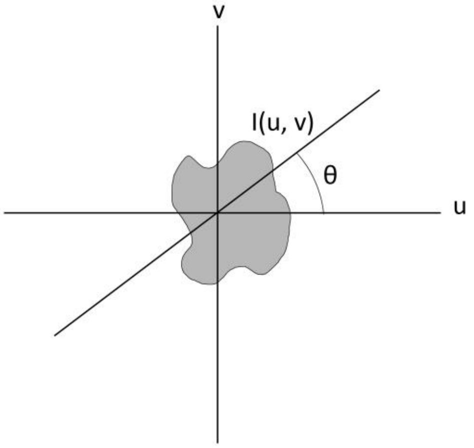

Figure 3-7- Fourier transform of a projection gives the Fourier transform of a slice of the image from which the projection was obtained from.

3.2.3 Filtered Back Projection

Filtered back projection is introduced to correct for the blurring by processing the original view (filtering) before they are back projected. Blurring is due to over sampling of the center of the image where the various projections overlap.

In essence, a filter function $|\omega|$ is applied to the projection before being back projected.[14]

$$I(x,y) = \int_0^{\pi} \left[\int_{-\infty}^{\infty} G(\omega,\theta)|\omega| e^{-i2\pi w\rho} d\omega \right] d\theta \tag{6}$$

The filter function filters out low frequencies (blurring) and attenuates high frequencies (features of image).

4. Experimental Procedure

4.1 Rigaku Smartlab X-ray Powder Diffractometer

4.1.1 Sample Preparation

As the hydration mechanism as a function of grain size is to be studied via XRPD, powder specimens were manually grinded via a mortar and pestle (fig. 4-1) to produce two different grain sizes. A fresh cylindrical block of C3S was provided by Tongji university on December 2015 then ground for use on 2nd February 2016.

The powdered C3S is held in a square recession on a glass slide of depth 0.2mm to reproduce a flat homogenous powder surface in accordance with the x-ray geometry (Bragg-Brentano) so accurate peak intensities over the θ-2θ range is obtained. Although the aim was to produce two different grain sizes, it found that the powder still had to be sufficiently fine in order to remain in the trench, else it would fall out upon little force to the glass. This meant that the sample holder carrying the 'big' powder grains had to be handled with care as to not disrupt flat surface. Compaction of the powder was prevented by using as little force as possible when drawing the flat edge (of the glass slide) over the powder (see fig. 4-3), however some degree of compaction is still unavoidable in order to create a flat surface so preferential orientation of the grains may still occur.

A make-shift mesh of aperture 70μm and 30μm was tested (see fig. 4-4) in an attempt to approximate particle sizes, however it proved too cumbersome to filter out any meaningful amount to use in a reasonable timeframe due to the small quantity of powder being dealt with. Both the large and small grains managed to pass through the both the 70μm and 30μm mesh to differing degrees, with the large grains requiring much more 'shaking' to pass through a small amount, whereas the small grains seemed to pass with more ease. This questions the homogeneity of the particle size distribution of the big grains, however from the TXM images seen later which showed a grain size of 50μm, from a batch grinded even more strongly than here, implies most of the particles here are larger than 30μm.

To produce the two grain sizes; the cement was continuously grinded and tested periodically to determine whether the powder was fine enough to remain in the sample holder without falling out while being handled and tilted. Once the upper limit to remain in the holder was determined, the batch of powder was separated in half and grinded further for several more minutes. The 'roughness' and resistance to grinding can also easily be felt under the pestle, and eventually dissipates with grinding duration.

Figure 4-1-Mortar and pestle to produce C3S powder specimens.

Figure 4-2- Sample holders of big and small grain size. Wrapped in cling film for water retention and protection of surface.

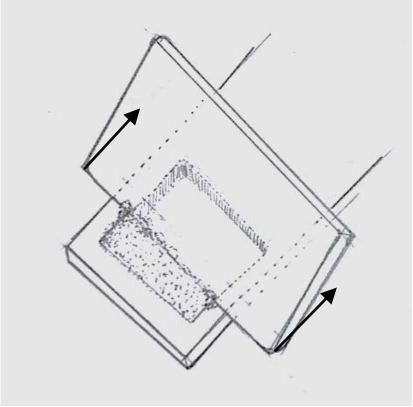

Figure 4-3: Illustration showing preparation of the flat powder specimen. A glass slide with edge flat against the sample holder draws the cement powder/paste across the square trough in single 'sweeping' motions.

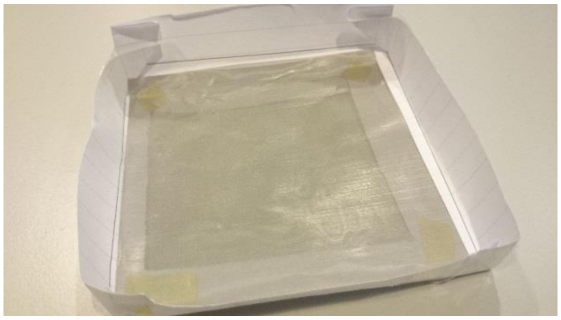

Figure 4-4- Make shift 30µm mesh. Too cumbersome to filter useful amounts

.

To prepare the hydrated samples, equal masses of the big and small grains were weighed out into separate beakers, and hydrated at a 1:2 water to cement ratio (tap water used to simulate industrial cement hydration), before being thoroughly mixed and spread onto the sample holders with the edge of a glass slide. Cling film was stretched over the sample to improve water retention (see fig. 4-2) as the sample reacts rapidly during the first few minutes. This was done approximately 5 minutes post hydration, and in hindsight, as will be discussed later, was possibly still too long.

4.1.2 Operation of the Rigaku Smartlab Diffractometer

X-ray Powder diffraction measurements over a span of 28 days was performed using the Rigaku Smartlab diffractometer under Bragg-Brentano geometry with a Cu-Kα radiation source of wavelength λ=1.5418Å [. The system is user controllable via the Smartlab guidance software to input the desired optical arrangement and measurement settings. For this experiment, the pre-programmed package "General (Bragg-Brentano focusing)" is chosen and walks the user through all the optical and sample alignments steps necessary for our flat specimen reflecting geometry. The non-detectable options include: -

- The Cu-Kβ nickel filter insert-able into the receiving arm (which is prompted by the software anyway). This is used to reduce the intensity of the Cu-Kβ line as the absorption edge of nickel has a greater wavelength than this. It should be noted that this does not affect the Cu-Kα2 line which is supposedly resolved from the Cu-Kα1 once PDXL fits the calculated peaks to the data. However, this is not always the case as will be apparent later in the results.
- The SC-70 scintillation detector is the correct option.

Figures 4-5 and 4-6 shows the Rigaku in its operating state and the optical configuration used for the Bragg-Brentano geometry. Scan settings used are as follows:

Incident slit	2/3 deg
Receiving slit 1	2/3 deg
Receiving slit 2	0.3mm
Length limiting slit	10mm
Tube voltage	45kV
Tube current	200mA

Table 4-1- Smartlab guidance settings

The samples were mounted on the sample holder shown in figure 4-6, and held in place by two clips. Sample alignment is carried out on a silicon reference powder sample at the start of each session, to check for any displacement of the height. The optical alignment had to be carried out at the start of each session as the components were frequently interchanged between Parallel beam and Bragg-Brentano geometry, hence zeroes any offset in the 2Θ and ω.

Figure 4-5: Rigaku Smartlab Diffractometer

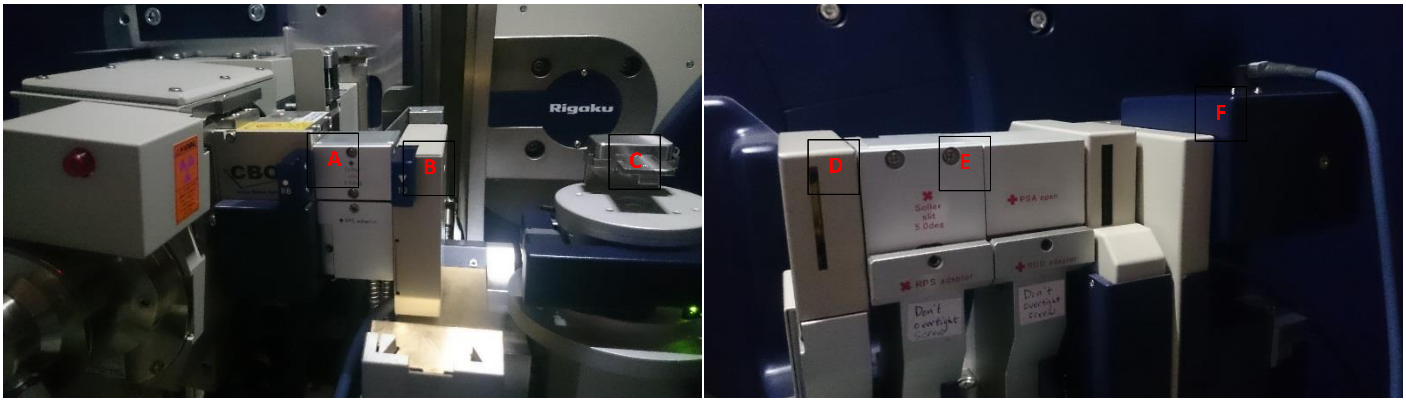

Figure 4-6: Incident arm: A: Soller slit 5deg. B:10mm divergent slit. C: Sample holder. Recieving arm: D: Cu-Kb filter slit. E: Soller slit 5deg. F: Scintillator detector, SC-70

Quantitative data is extracted from the diffraction patterns using PDXL: Integrated X-ray powder diffraction software. Calculated peak shapes, pseudo-Voigt functions [16] are automatically fitted to the experimental peaks, returning the desired peak positions (2θ), Integrated widths, Integrated intensities and estimated standard deviations. In the lab computer version of PDXL, only the Autosearch function was enabled for use which returns the most likely chemical formula of the sample based on reference data base patterns (ICDD PDF/COD) compared with the experimental data. This is a very useful tool as not only does it verify the purity (or impurity) of the unhydrated C3S, but matches any potential hydration products to unfamiliar peaks.

Measurement Timeline:

Scan ranges Θ-2θ of 5-90° were carried out where possible with minor adjustments depending on time constraints due to the user schedule. Scan lengths were increased to 2°/min after the first day as the intensities of the C3S peaks are expected to decrease with hydration time. This gives less noisy data as the intensity counting statistics is increased. The standard deviation of an intensity varies as $\sqrt{N}$, N is the photon count [17]. These measurements apply to both grain sizes.

Hydration time	**Scan speed (deg/min)**	**Step width (deg)**
1hr	4	0.02
2hr	4	0.02
3hr	4	0.02
4hr	4	0.02
5hr	4	0.02
6hr	4	0.02
1d	2	0.02
2d	2	0.02
8d	2	0.02
9d	2	0.02
11d	2	0.02
15d	2	0.02
28d	1	0.01

Table 4-2- Slower scan speeds used for less noisy data due for lower intensity peaks.

4.2 Transmission X-ray Microscopy (TXM) – Xradia 810 Ultra XRM

In addition to the XRPD measurements, the opportunity to use the Xradia Ultra x-ray microscope on the hydrating C3S grains arose. The field of view of the microscope is 65m at 150nm resolution [18] therefore a grain smaller than this had to be prepared. Measurements were completed for 5 days and 28 days post hydration.

A piece of the C3S block was removed and grinded as finely as possible using the mortar and pestle similarly to the XRPD samples, and hydrated with a 1:2 w/c ratio. Specially prepared capillary tubes of 100µm and 1mm diameter (fig. 4-7) were used to store the hydrated cement paste. The opening of the tubes was submerged into the hydrated cement and thus the paste flows into the tube via capillary action. It was discovered later however that the 100µm was sealed at the opening therefore no cement paste had entered it.

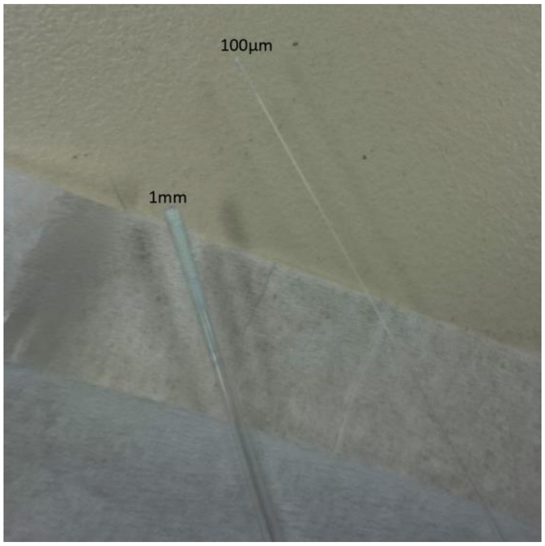

Figure 4-7- 1mm and 100micron capillary tubes.

N.B: It must be noted that I personally did not have permission to operate the equipment in the microscopy lab, therefore all the following procedures were carried out by trained persons while I spectated.

After 5 days of curing, the paste was extracted from the tip of the 1mm capillary tube using a pin. Epoxy glue was applied to the very tip of a pin, and using an optical light microscope, the smallest grain found was fixed on. This proved to be a challenging task due to the limited resolution of a table-top microscope and the precision of movement using hands. To ensure the grain was sufficiently positioned in the correct orientation, and within the field of view, a higher resolution microscope was projected to a monitor (fig. 4-8) which enabled the diameter of the grain to be determined. A thin wire was used to tilt the grain to the correct orientation if necessary. The grain chosen for measurements had a horizontal diameter of approximately 45µm hence was determined fit for use.

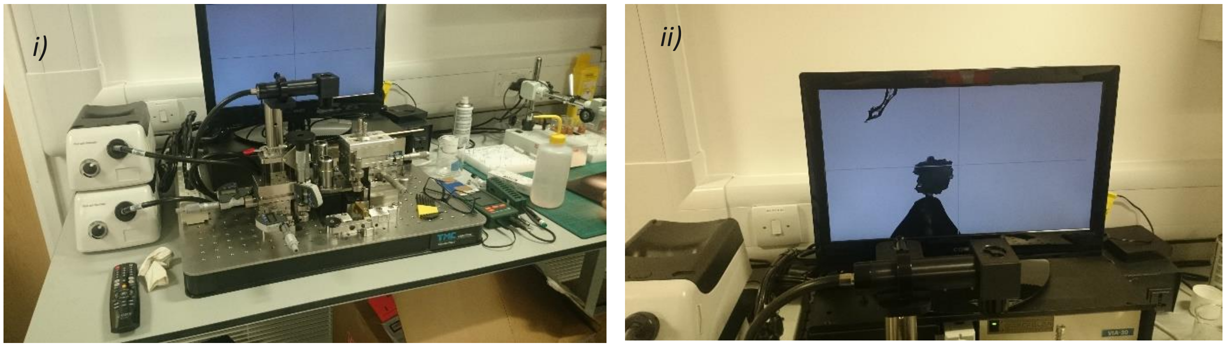

Figure 4-8- i) Fibre-optic illumiated microscope set-up. Sample mounted on movable base with digital calipers. ii) Image projected to monitor. Grain affixed to tip of pin.

TXM settings: The Absorption contrast imaging setting was used in the measurements. This generates the images (or rather shadows) based on the different attenuation properties of the matter in the sample. This was chosen as it is the pore structure within the C3S grain we are interested in seeing which significantly differs in density to the C3S.

Phase contrast imaging, the other available mode of operation, is possibly more advantageous in scenarios where finer details such as edges of similar transparency regions, as it detects the phase-shift of the outgoing x-ray beams based on the fact that different materials have differing refractive indexes [19]. This may have been a better option if it were the CSH surface layer we were interested in imaging as that is of a different composition.

Operation settings are listed below:

	Binning	No. of projections	Exposure
5 Days- 2 scans	1,2	721, 721	32
28 Days	1	721	35

Binning is the combination of adjacent pixels to a single pixel which increasing the signal to noise ratio at the expense of image resolution. Below are two slices from identical positions within the grain, sampled at binning 1 and 2. [20]

It is immediately apparent that binning 1 gives the clearest image hence this was also used for the 28 day measurements.

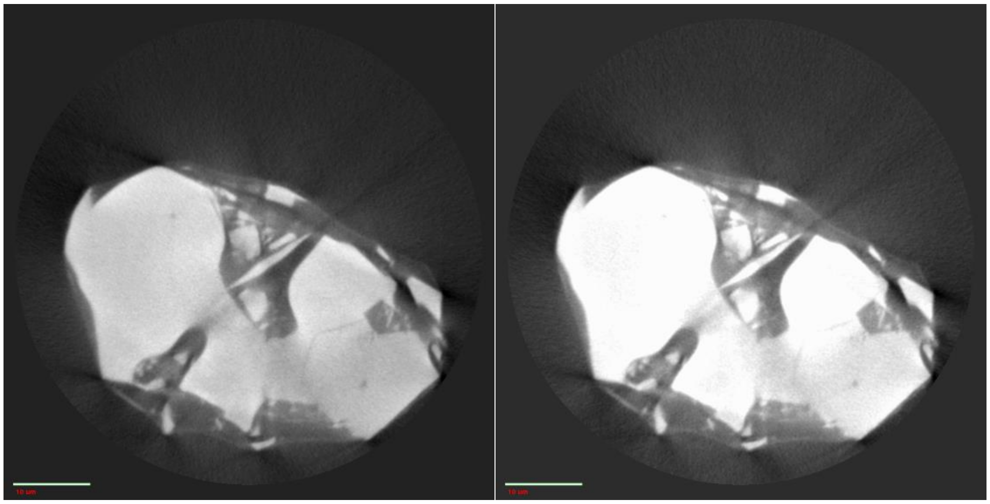

Figure 4-9- C3S 5 days: Same slice position with binning 1 and 2. It is apparent that binning 1 gives sufficient pixel intensities without losing detail on the finer structure while binning 2 is too bright.

5. Data Analysis Techniques

5.1 Williamson-Hall method

The Williamson-Hall method is based on the idea that broadening of diffraction peaks can be separated in size and micro-lattice strain effects. Size related broadening occurs when a crystallite domain is so small that there are insufficient Bragg planes for coherent diffraction to occur. For $\theta \neq \theta_B$, a large crystal has 'infinitely' many planes so waves out of phase with the first plane will all destructively interfere with subsequent planes out of phase by 0.5λ, so there will be no net intensity around θ_B. The Scherrer equation [21] relates the average crystallite size to the broadening as:

$$\beta_D = \frac{K\lambda}{D\cos\theta} \tag{5.1}$$

D= average crystallite size; K= Scherrer constant, 0.9 for spherical and 1.2 for cubic; β_D=broadening, θ= angle of diffraction.

Lattice-strain broadening occurs when external forces on a crystallite causes inhomogeneous distortions to the lattice parameters, thus interplanar spacing d. The peak is broadened for a powder sample with a distribution of d values about the unstrained value. This can be seen with Bragg's law, where d is inversely proportional to $\sin\theta$. Lattice strain can occur as a result of external forces acting on the anhydrous cement grain, due to the formation of hydrates along the surface. **Chemical shrinkage is due to the reduction in volume of the grain due to hydration. When water within a pore dries out**

The strain, ε is related to the broadening, β_ε via the Stokes-Wilson equation [22]:

$$\beta_\varepsilon = 4\varepsilon\tan\theta \tag{5.2}$$

5.1.1 Instrumental Broadening

There is also the instrumental broadening contribution to consider, which are inherent to the system. This includes axial divergence due to slit widths, unresolvable $K\alpha_1/K\alpha_2$ peaks, sample displacement error. This can be determined by using a crystal sample of sufficient large domain size, and no inherent micro lattice strain. Any broadening observed in the diffraction pattern is then assumed to be purely due to instrumental effects.

In this experiment, a standard Silicon reference powder was used as it fits these conditions.

The integral breadths were used as the broadening parameter as this was the intended value [23] rather than the FWHM which is also commonly used. The integral widths and 2θ peak positions were recorded six times from 0-90° and averaged to create an instrument broadening curve, which the polynomial equation could be extracted from (fig. 5-1).

The corrected broadening due to size and strain effects alone, β_r is then obtained by:

$$\beta_r = \beta_{o-}\beta_i \tag{5.3}$$

Where β_o is the observed broadening (from experiment), and β_i is the instrumental component (from silicon).

However, for a Gaussian line shape, equation 5.4 becomes [9]:

$$\beta_r{}^2 = \beta_o{}^2 - \beta_i{}^2 \tag{5.4}$$

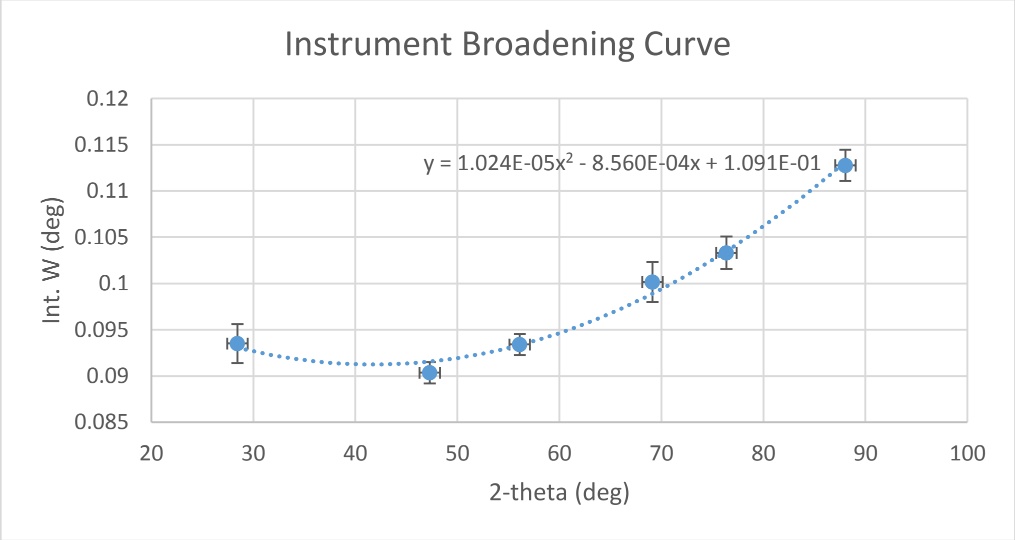

Figure 5-1: Instrumental broadening curve.

5.1.2 Williamson-Hall Plot

After subtracting the instrumental broadening, the broadening can then be deconvoluted into the size and strain effects via the Williamson-Hall method as follows:

$$\beta_r = \beta_\varepsilon + \beta_D \tag{5.5}$$

$$\beta_r = 4\varepsilon \tan\theta + \frac{K\lambda}{D\cos\theta} \tag{5.6}$$

$$\beta_r \cos\theta = 4\varepsilon \sin\theta + \frac{K\lambda}{D} \tag{5.7}$$

Which is the form of a straight line $y = mx + c$, where $m = 4\varepsilon$ and $C = \frac{K\lambda}{D}$.

5.2 Image processing with ImageJ

The raw projections data were converted to .tiff image format and viewed with image processing software ImageJ [24]. These slices could then be stacked together reconstructing a 3D model of the grain. By manipulating the slices prior to reconstruction however, such as highlighting the areas of interest using the “Adjust threshold” tool, the surface and internal structure could be viewed in great detail. Z-projections are useful for viewing overall changes in pore sizes.

RGB images are converted to 8-bit greyscale images. In 8-bit images, there are $2^8 = 256$ pixel intensity values, with 0 being black and 255 being white. The Adjust threshold tool allows selection of intensities within a user defined range.

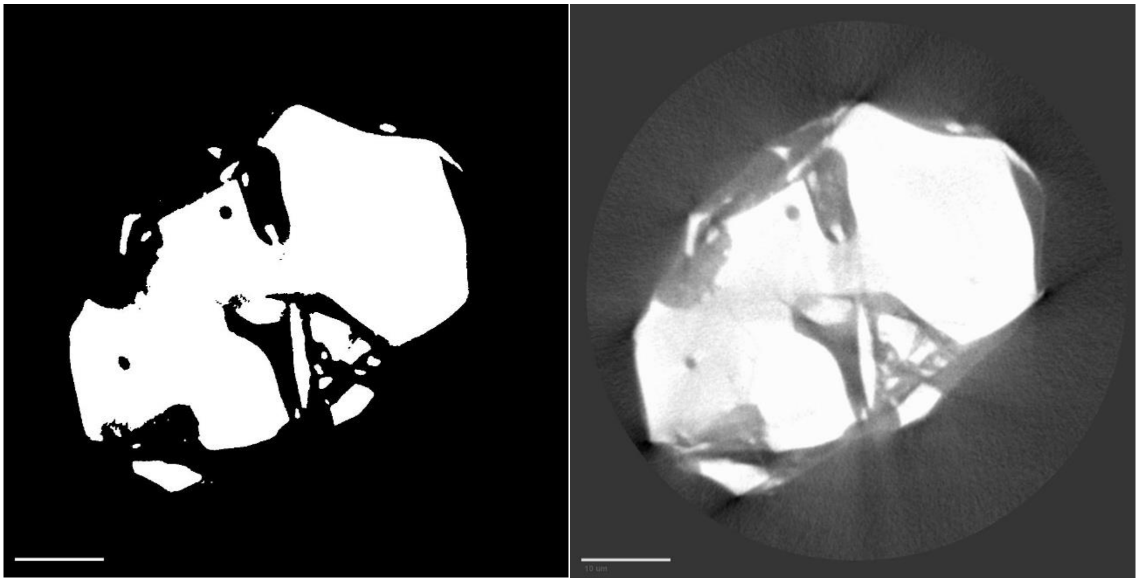

Figure 5-2: 28day Slice with 0-202 thresholding (left). Unedited slice (right).

To reconstruct the grain surface, the solid mass along the same plane is highlighted white, so the pores are still visible (fig. 5-2). The pores can also be reconstructed from inverting the selection when the mass is highlighted black.

Figure 5-3 shows the reconstruction with different thresholding values. 500 slices were used for both datasets as any more becomes too computationally intensive for reconstruction within reasonable timeframe.

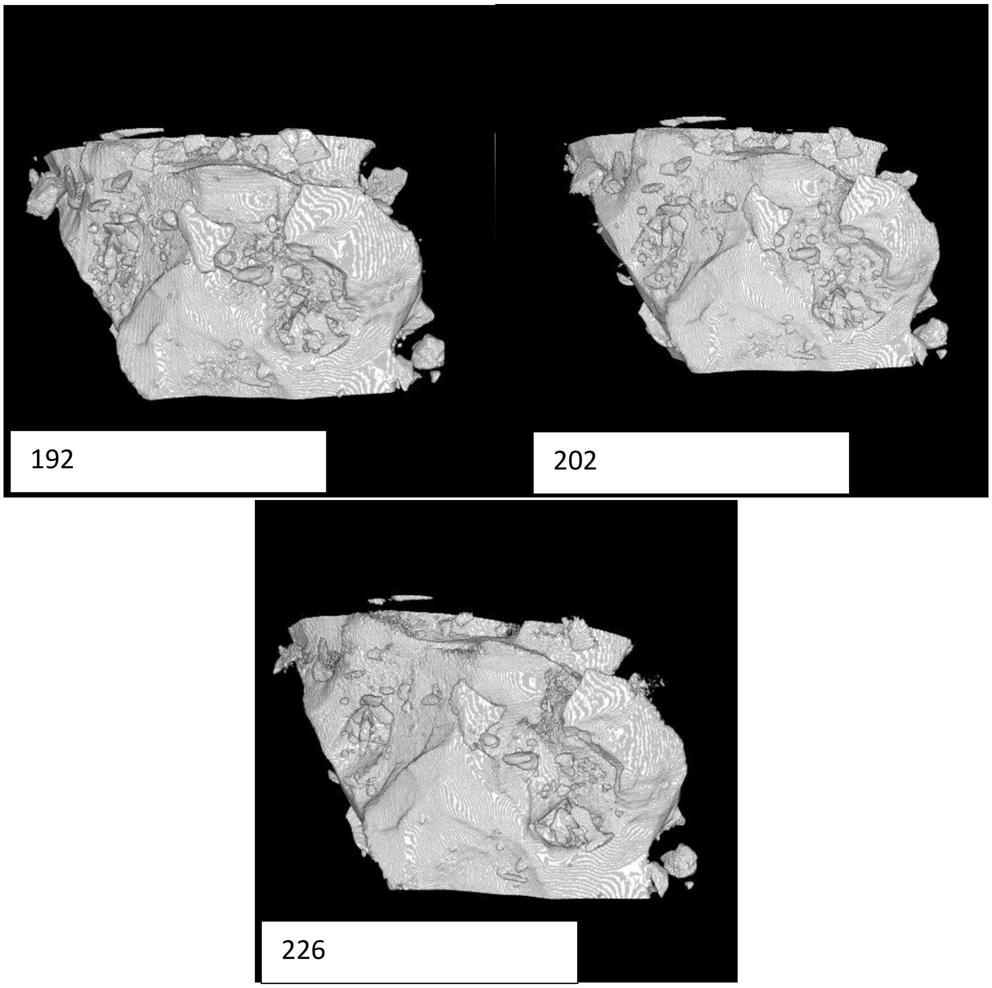

Figure 5-3: Different threshold values.

6 Results and Analysis

Average crystallite size and lattice strain has been obtained over the 28 day measurement span for both small and big grain sizes via the WH method. This is analysed In conjunction with the diffraction patterns and microscopy data. Where results deviate from theory, possible sources of uncertainties will be discussed.

TXM data were obtained for 5days and 28days of hydration. Slices through the cross-section are qualitatively analysed, and have been reconstructed into 3D models using ImageJ.

6.1 C3S Small Grains

Williamson-Hall analysis

The diffraction peaks chosen for the Williamson-Hall plots were done by extracting the integral widths from the diffraction patterns in PDXL and selecting the peaks associated with Tricalcium Silicate (which were identified by PDXL 'Autosearch' function as Hatrurite, formula Ca9O15Si3). After plotting and applying a least squares fitting for the 8 most intense peaks, it was found that the broadening did not vary linearly as predicted due to several reasons. Calculated peaks and hence integrated widths from PDXL were not fitting correctly on some peaks. i.e. Seperation of $K\alpha_1$ and $K\alpha_2$ peaks, overlapping of adjacent peaks, lattice distortion effects.

A high intensity peak at ~29.4° has unknown shoulder on left of the peak, which PDXL attempted to deconvolute into two peaks for some patterns and not others. This results in significantly different integral width values as can be seen in figures 6-1 and 6-2. The ~56.6 peak similarly could not be resolved consistently due to overlapping peaks.

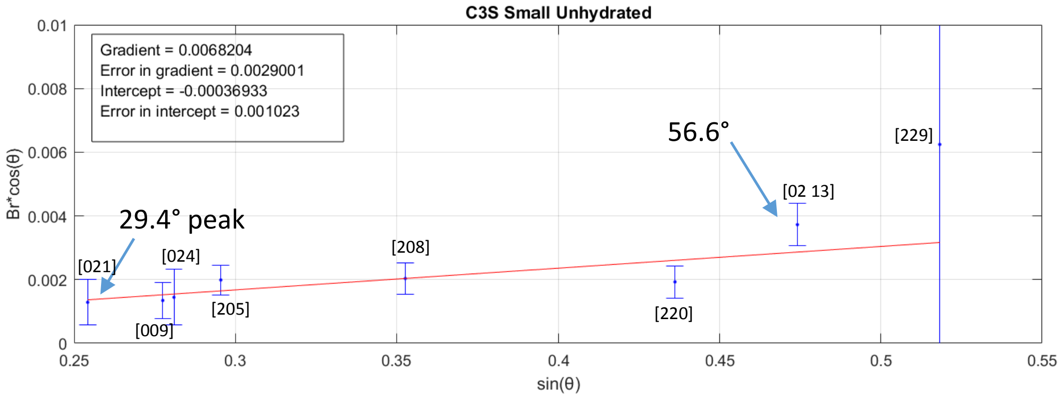

Figure 6-1: C3S Small unhydrated WH plot 8 largest peaks. Miller indices assigned to each peaks, obtained from ICDD PDF reference card for Hatrurite.

The ~62.4 and 51.7° peaks have significantly higher and lower broadening respectively relative to the best fit line. This variance in broadening could arise from preferential orientation of the particles due to uniaxial pressure applied to the powder during flattening. Another possibility is anisotropic strain broadening which is strain being directionally dependent [25], [26].

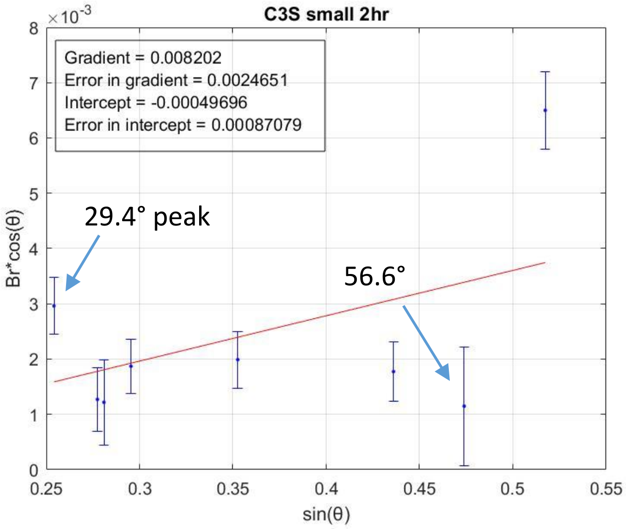

Figure 6-2: C3S small 2hrs

The size and strain have been plotted over the 28 day timespan in figure 6-3. The four peaks used in the plots are circled in figure 6-1, corresponding to the ~32.2, 32.6, 34.3 and ~41.3° peaks. These were chosen on the basis that they consistently lied along a straight line, and PDXL had the least trouble fitting calculated peaks to them. For direct comparison of size and strain for across measurements, all points must be similarly fitted as one inconsistently fitted point will heavily skew the gradient and intercept. Broadening should increase with 2θ (according to the Scherrer equation). From figure 6-1 and 6-2 (and further WH plots in the appendix), one can see the parabolic nature of the points. As we are interested a linear fitting, only those which lie about the line of best fit are considered for use.

Intercepts obtained returned negative values which are non-physical, so only qualitative trends can be made from the results.

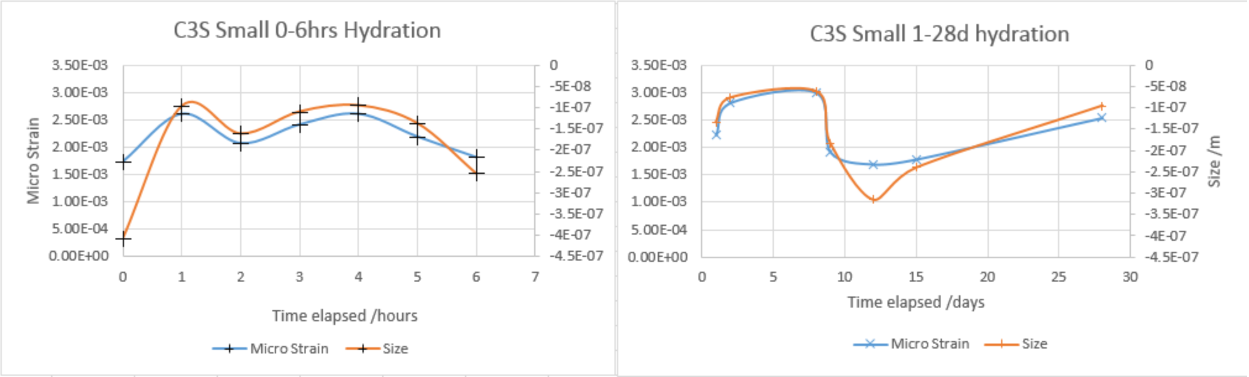

Figure 6-3: C3S small. Lattice micro-strain and average crystallite size plotted over 28 day measurement span.

The unhydrated measurement is an anomalous result, as it is physically improbable for the crystallite size of the C3S to increase after hydration. As two separate sample holders were used for the unhydrated and hydrated sample, this may have been caused by differences in pressure applied during the sample preparation inducing more strain. The integral breadth does not depend on the quantity of powder, which only effects the peak intensity, thus any perceived broadening may be strain related.

From 1 hour to 6 hours, the size and strain remained relatively constant, increasing and decreasing by a similar amount. Comparing this to the change in intensity of the major C3S peaks, the peaks fall to around 75% of their original integrated intensity on average and remains the same to 2 days.

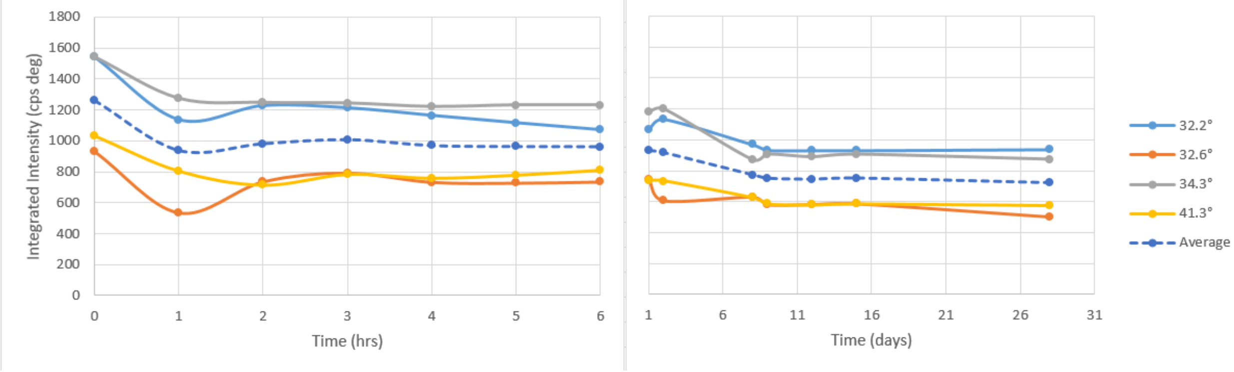

Figure 6-4: Integrated intensity of four major C3S peaks over 28 days of measurement.

The size and strain increase and decrease proportionally throughout the 28 days. This may instead indicate that one of the effects is dominant, as in theory, as the grain size decreases, this should correlate to an increased lattice strain and vice-versa.

CH should fully crystallise out within 24 hours, however no new peaks were observed. The only change appeared at 1 hour where an amorphous hump appeared around 17.9 (signature peak of CH) with two broad humps on either side. The two humps may be caused by extremely small particles of CH (in solution) being a different phase to the crystallised CH, however this is questionable as the intensity of the humps remain constant even after CH crystallises out as will be seen below.

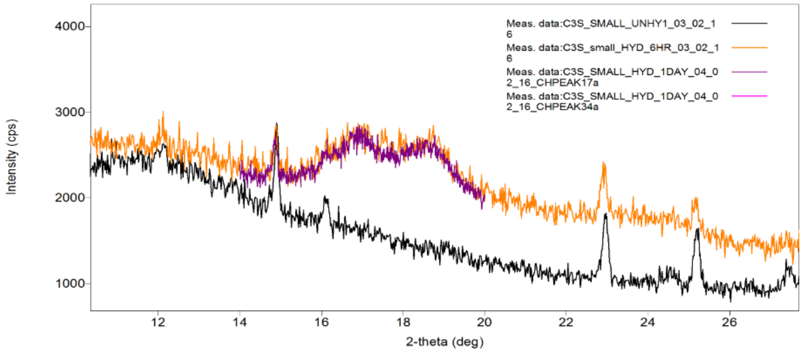

Figure 6-5: Broad amorphous hump around 17.9°.

As there was still no visible CH peak after 5 days (figure 6-5), and no noticeable changes in peak intensities; on day 8, the sample was rehydrated by dropping 100μL of water with a pipette onto the sample, and replacing the cling film immediately.

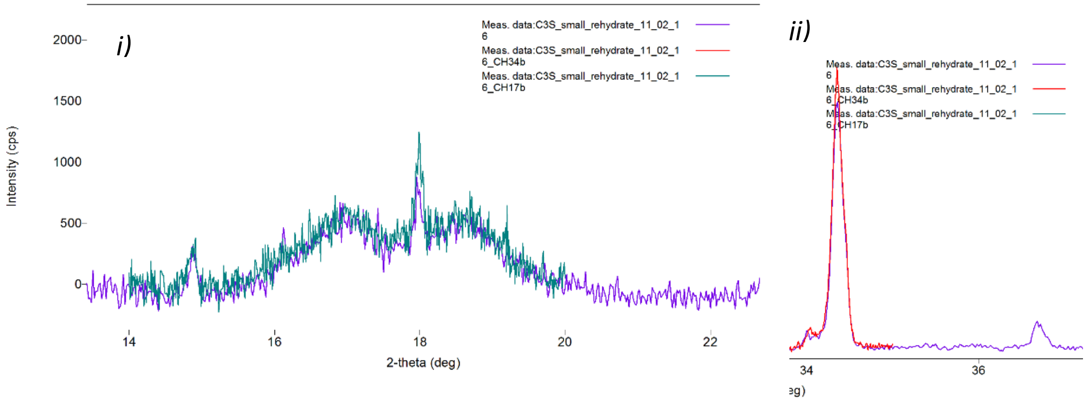

Figure 6-6: CH peak at 4 hours and 5 hours post rehydration, emerging at i) ~17.9° and ii) ~34°..

As seen in figure 6-6, two signature CH peaks at 17.9° and 34° emerge indicating a crystallisation of CH from the solution. The WH plot also shows an immediate decrease in lattice strain and size of the C3S between day 8 and 9 where the portlandite peaks reach a maximum intensity (figure 6-7). This could possibly correspond to a fracture within the grain due to dissolution and creation of pores within the grain, resulting in smaller domain sizes and thus release of lattice strain.

However, if the lattice strain is due contact forces between the C3S and hydration products, one would expect a larger difference (increase) in lattice strain prior to day 8 which is not seen, though this may indicate no hydration products formed yet. If the strain is due to shrinkage of the pores as the water dries out, maybe the increase in strain from 6hour to 2days indicate the loss of water, followed by a plateau between day 2 and 8. More study is required. Integrated peak intensities also decrease by ~10% and remain as such to 28 days.

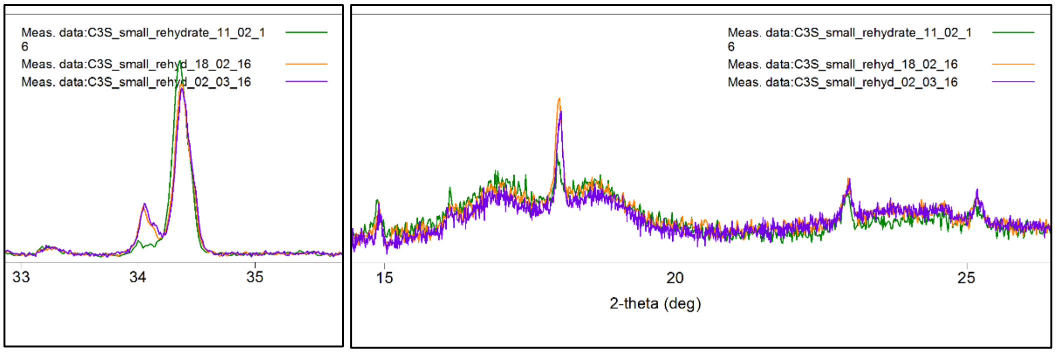

Figure 6-7: Maximum CH peak intensity reached at day 9, remains the same at 18d.

Green: rehydrated@8d. Orange: 15d. Purple: 28d

6.2 C3S Big Grains

Similar analysis was carried out for the big grain sizes. Lattice micro-strain and average crystallite size are plotted against time in figure 6-8. Again the unhydrated point at t=0hrs will be considered an null result.

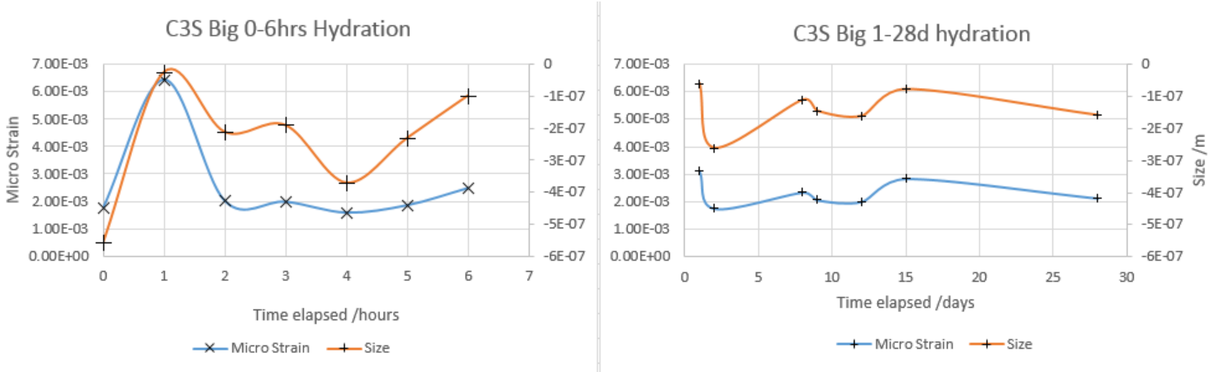

Figure 6-8 C3S big. Lattice micro-strain and average crystallite size plotted over 28 day measurement span.

The same peaks at ~32.2, 32.6, 34.3 and ~41.3° were again used.

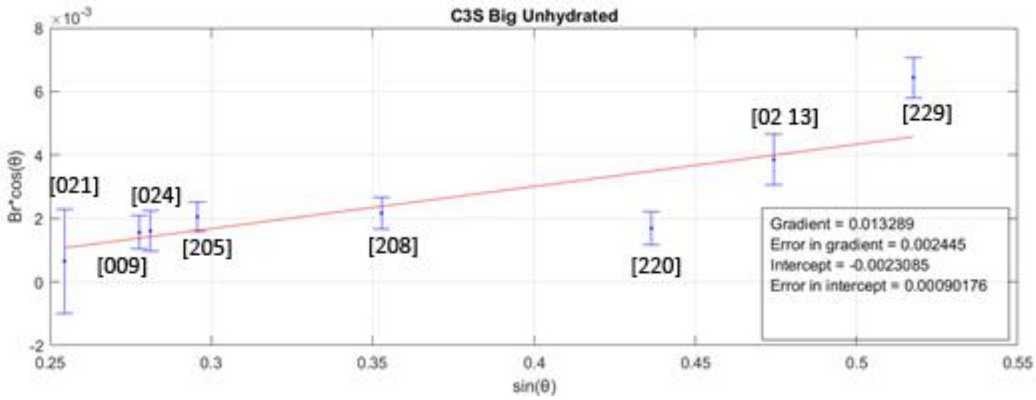

Figure 6-9: WH plot of unhydrated big grains

It is more difficult explain the trend here than for the small grains. The size fluctuates erratically but ultimately returns to a similar position at 28 days. The lattice strain remains proportional to the size between 1 and 28 days. Size broadening for the big grains should be negligible, unless the grain contains small domains less than 1micron in size [9], therefore strain broadening should be the dominant effect here. The Williamson-Hall plots all follow a similar distribution, with the [220] and [229] planes indicating a non-linear broadening in the crystal similarly to the small particles.

As the lattice strain remains largely constant throughout the 28day span, the Scherrer size which ignore the strain broadening component, can be plotted against time:

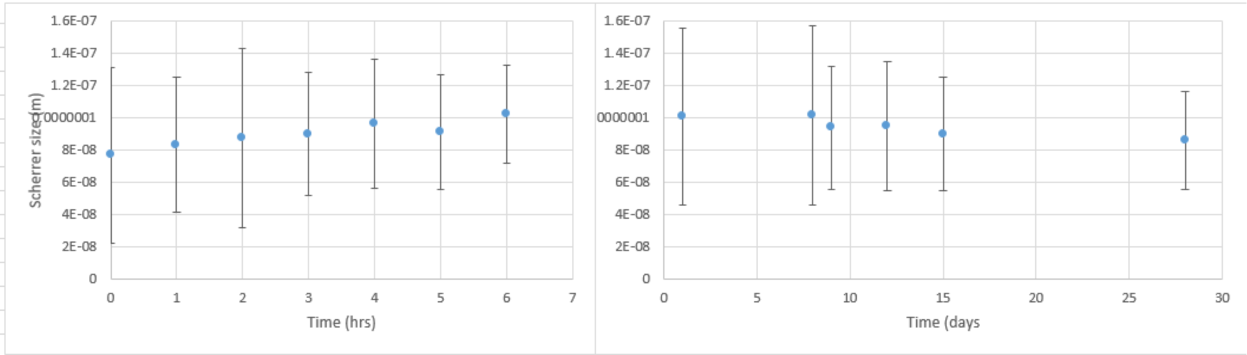

Within the first 6 hours, there is a gradual increase in size up to 1.3 time the initial value at 6 hours, and remains the same to day 8. After day 8, the size gradually decreases to about 1.1 times the initial value. The error bars are sufficiently large that one could also fit a straight line and assume constant size.

In the initial 6 hours, the integrated intensities drop to about 60% of the initial value, which is 15% lower than the small grains and remains relatively constant throughout to 28 days.

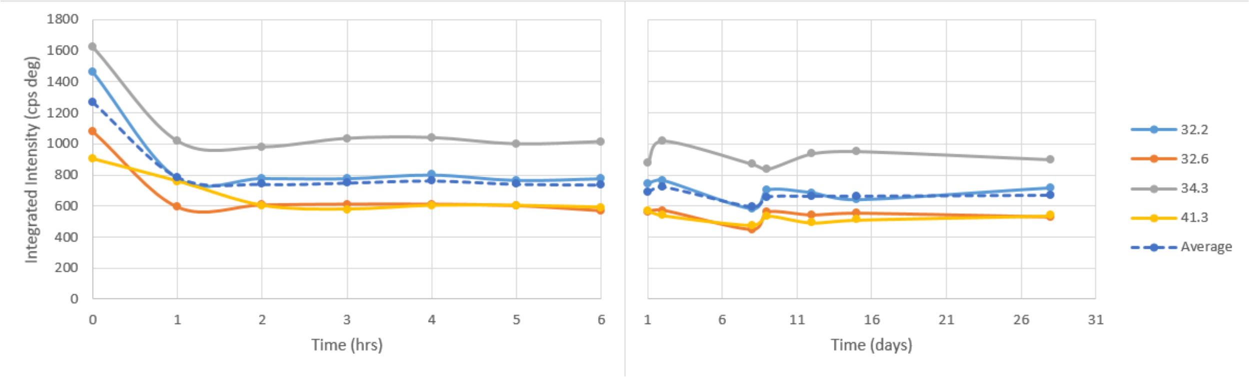

Figure 6-10: Integrated intensity of four major C3S peaks over 28 days of measurement.

Both particle sizes reach a plateau between initial and one hour of hydration. This could mean both solutions are saturated from the dissociate of C3S into ions, and thus, enter the induction period. The end of the induction period is indicated by the crystallisation of CH into portlandite.

The greater decrease in peak intensity could correspond to more C3S dissolving for the big particles such that CH reaches maximum saturation and crystallises out. This can be seen in figure 6-11, where the portlandite peak reaches a maximum at day 1, even after rehydration of the sample at day 8.

There is more dissolution of C3S here compared with the small powder sample within 1-6hours possibly due to the ratio of water present differing. During sample preparation, water may have evaporated during the initial hydration, as the cling film was not applied fast enough to prevent water loss. More water was lost for the small powder sample due to the more rapid reaction rate.

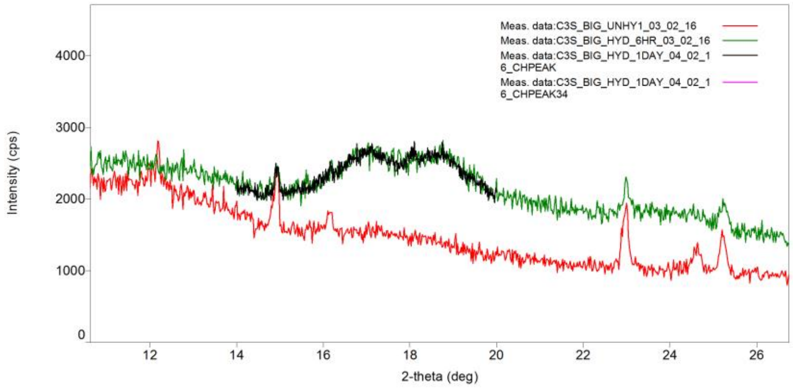

Figure 6-11: Small portlandite peak which is the maximum. Black: day 1. Green: 6 hours. Red: unhydrated.

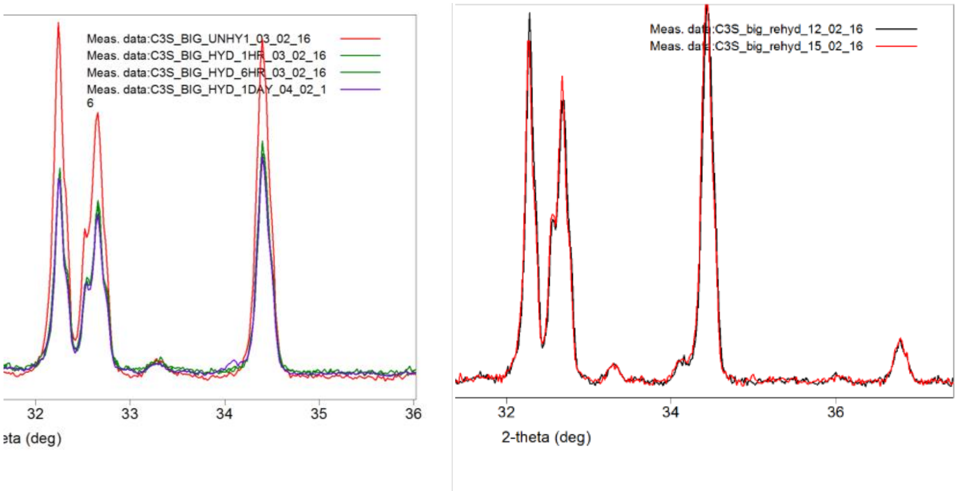

Figure 6-12: ~34° CH peak shows minimal change from 1day (left) to post rehydration (right).

Observations

The delayed induction period with the small grains prior to rehydration may supports the idea that the rate of dissolution is proportional to the surface area exposed to water though. One theory is, higher concentrations of silica results in the nucleation of CH is being inhibited even when the CH is super saturated (Barnes, Bensted p66 [2]). Once the sample was rehydrated though, the concentration of C3S decreases, and CH increased in the solution thus portlandite was allowed to form, which was seen in figure 6-6.

With the big grains, a crystallisation of CH was never seen to any significant degree, and remained largely the same even post rehydration. There is a marginal degree of crystallisation present at day 1 which was not seen with the small grains. This means the CH was able to crystallise out of the solution, thus CH nucleation was not inhibited, therefore implying the rate of dissolution in this theory would be lower; again agreeing with the idea of surface area exposed is proportional to rate of reaction.

However, experiments have shown that the ‘smoothness’ of the grain surface is also a factor. Annealed powders have shown longer induction periods [27] than non-annealed samples. In this experiment, small grains were grinded longer therefore more surface defects may have been created.

Looking at the WH plots for both grain sizes, there appears to be some uniaxial strain along the [220] and [229] planes. From the equations 5.2, broadening is proportional to the lattice strain. The [220] plane has less strain, and the [229] plane has more strain.

6.3 TXM image processing

Due to the limitted computer processing power, a maximum of 500 stacks was possible for the 3d viewer. For the 5 day scans, a threshold of 145 was applied to all slices. For 28 days, 192 was applied. These were judged to give sufficient surface detail without hiding pore openings.

Externally, there is little change in the surface of both measurements (fig 6-13/14). The grain size at 5 days and 28 days both remain about 50µm along the longest horizontal width (fig. 6-15). Pore openings on surface remain the same size after 28days (fig 6-16). Previous experiments have shown the reactivity is lower for annealed grains [27], [28]. In the figures, the surfaces surrounding the pore openings seem to be unsmooth and indented. Whether this was present prior to hydration or due to hydration is unknown though.

In figure 6-17 and 6-18 we can see a pore penetrating through the whole grain. Between 5 and 28 days there is no discernible change in the pore structure from comparing all the slices in ImageJ. For example, figure 6-19 shows identical features for 5 and 28days. This could be due to an absence of water in the grain thus hydration has halted, or the hydration has slowed down to a point where it cannot be seen within the time frame. The single grain was stored at room temperature in air so evaporation may be the cause. Looking through the cross sections, the crystallites within the grain seem to vary in size, with the largest up to several microns in size (fig. 6-20).

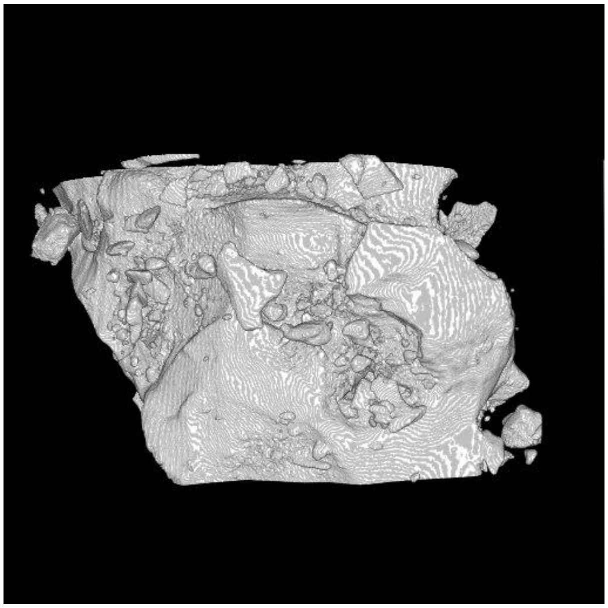

Figure 6-13:28d 3D reconstruction

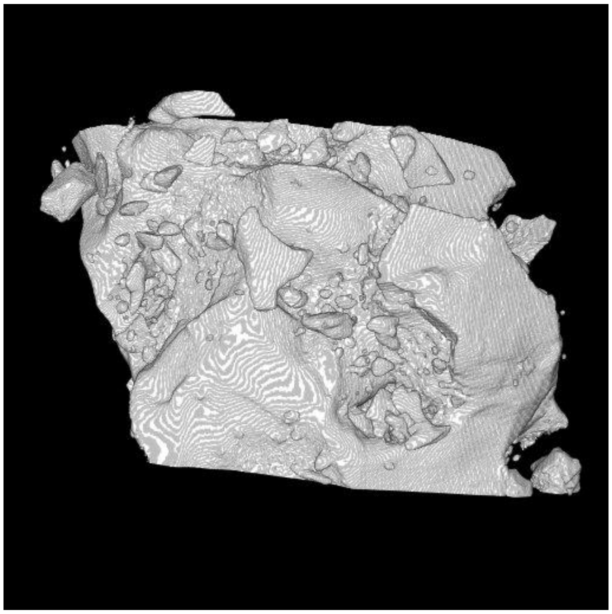

Figure 6-14: 5d 3D reconstruction.

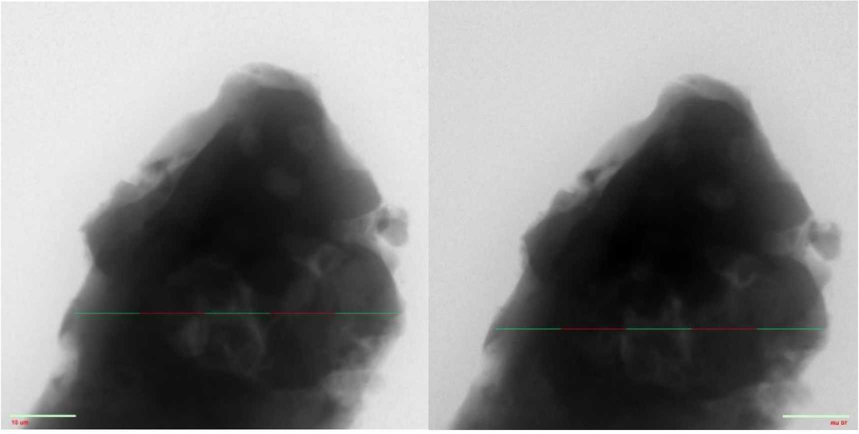

Figure 6-15: both grains show no noticeable change in grain size. Coloured segment is 10µm each= 50µm across.

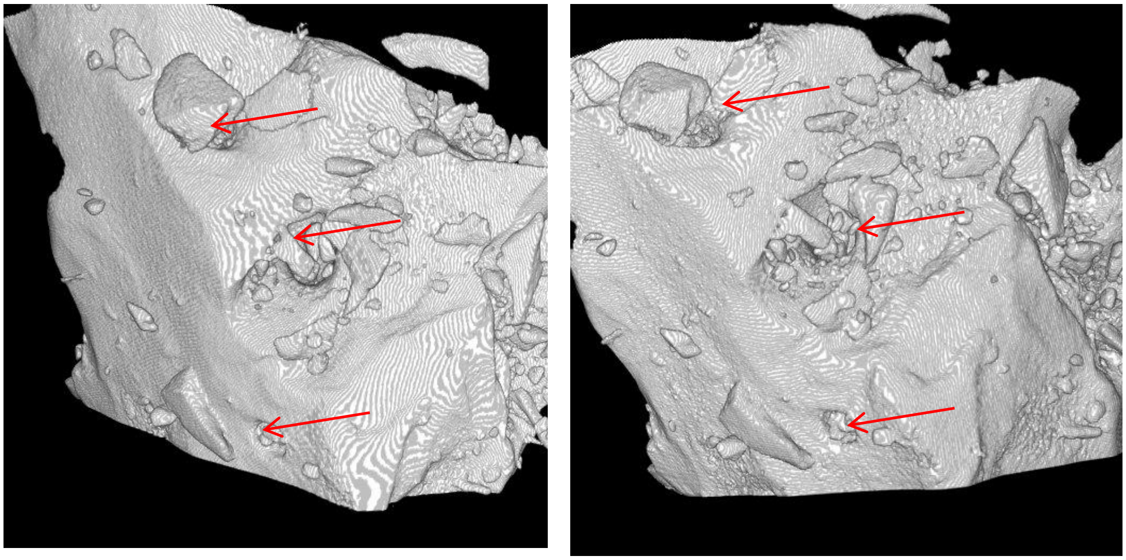

Figure 6-16: left, 5d, right 28d. Pores openings labelled.

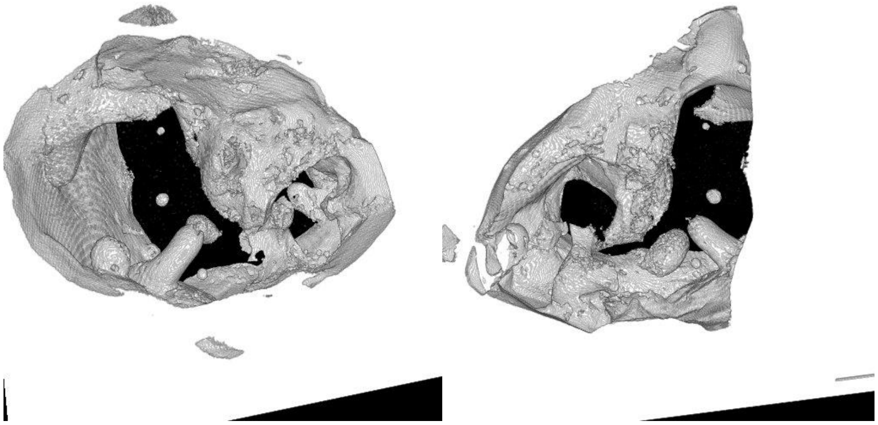

Figure 6-17: pore connectivity at 5d

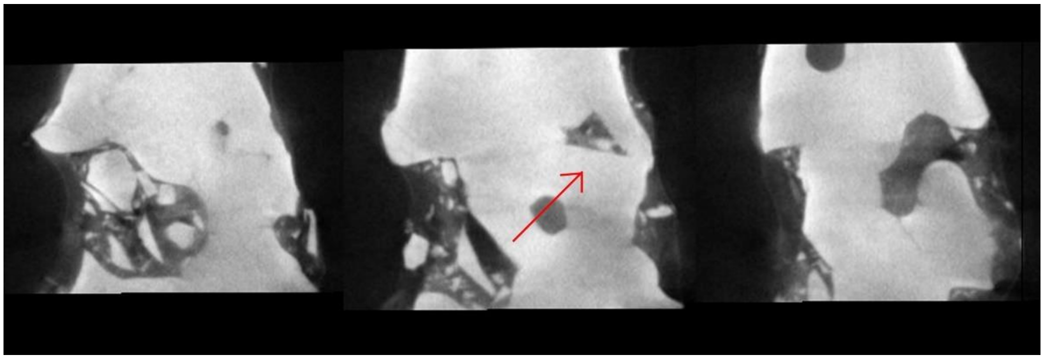

Figure 6-18: 5d: Orthogonal cross section. Pore connecting across grain. Slices deeper from left to right.

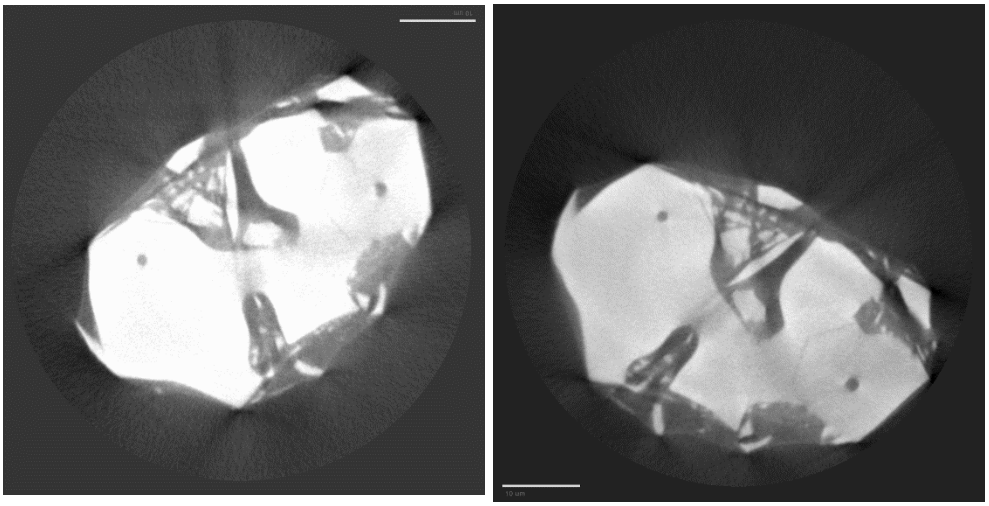

Figure 6-19: left: 5d. Right: 28d. No discernible change in pore size or structure.

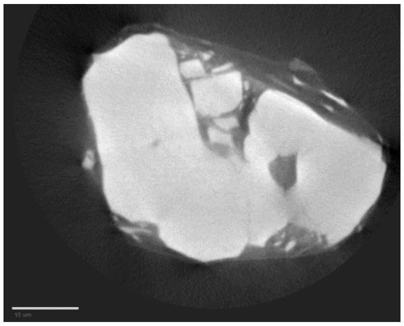

Figure 6-20: white bar=10µm. Large crystallite on top several microns across.

7 Conclusion

For the smaller grains, hydration after one hour seemed to have slowed down, or halted after the initial appearance of the amorphous CH peak until rehydration. This was determined to be due to an insufficient w/c ratio, probably due to evaporation during sample preparation, despite a 1:2 w/s used.

On the other hand, the bigger grains saw a marginal crystallisation of CH at 1 day, implying the induction period had ended. Upon rehydration, for the small grains, the CH is seen to crystallise into portlandite and grow during the 4hr and 5hr post hydration measurement slots, though from the size of the peaks and growth, most likely started crystallising earlier. Therefore, prior to rehydration, it is possible the pause in hydration occurred after a significant quantity of CH was already formed, also indicated by the amorphous CH peak. Portlandite growth was at a maximum when measured 1 day later, and significantly larger than for the big grains. This implies some suppressant factor is involved.

From the C3S peak integrated intensities, the small grains exhibit another decrease after rehydration, whereas the big grains remained constant as expected. Possibly because small grains exhibit

Between 8 and 9 days, the lattice-strain shows a sudden decrease for the small particles. This coincides with the precipitation of portlandite.

From the TXM data, no perceivable change was observed from comparing all the projection slices between 5d and 28d post hydration. It is well known that C3S continues hydrating past 28 days [1]. This could be due to the same reason the small particles ‘stopped’ hydrating, as there was no more water left for hydration. The grain was mounted on a pin, and stored upon a counter in a plastic housing at room temperature, without any preventative measures against moisture loss. Ideally if the grain continued hydrating, it would have been interesting to see if the grain size changes, thus could be compared to the Williamson-hall, if the crystallite domain size actually changes, or if broadening is sole strain dependent.

Regardless, pore connectivity was observed, as well as several other ‘in progress’ smaller pores. Pore entrances were surrounded by uneven surfaces, though unknown if they existed prior to hydration. It has been shown that annealing to remove surface defects reduces the heat released during hydration [27].

From the Williamson-Hall plots, only 4 points within a limited 2θ range were used. This was unfavourable, as the calculated peaks by PDXL at higher angles were inconsistently deconvoluted, sometimes where no separation of peaks was necessary (i.e. 29.4 very intense peak) resulting in inconsistent broadening values. Manual fitting of peaks could be done in the future. Additionally, the broadening did not increase as a linear function according to the WH method, but rather exhibited parabolic fit. This implies the presence of some preferential orientation of the lattice strain [25]. Alternative methods such as the modified Williamson-Hall method which accounts for strain anisotropy causing the scattering could be considered in the future [29].

References

[1] H. Taylor, “Cement chemistry : 2nd edition,” *Thomas Telford Publ.*, 1997.

[2] P. Barnes and J. Bensted, *Structure and Performance of Cements, Second Edition*, vol. 2002. 2002.

[3] M. N. De Noirfontaine, M. Courtial, M. De Noirfontaine, F. Dunstetter, G. Gasecki, and M. Signes-Frehel, “Tricalcium silicate Ca3SiO5 superstructure analysis: a route towards the structure of the M1 polymorph,” *Zeitschrift für Krist.*, vol. 227, no. 2, pp. 102–112, 2012.

[4] Y. SAKALLI and R. TRETTIN, “Investigation of C $_3$ S hydration by environmental scanning electron microscope,” *J. Microsc.*, vol. 259, no. 1, pp. 53–58, 2015.

[5] S. Garrault, T. Behr, and A. Nonat, “Formation of the C-S-H layer during early hydration of tricalcium silicate grains with different sizes,” *J. Phys. Chem. B*, vol. 110, no. 1, pp. 270–275, 2006.

[6] Peter Hewlett, *Lea’s Chemistry of Cement and Concrete*, vol. 4. 2003.

[7] S. Mindess, J. . Young, and D. Darwin, *Concrete*, 2nd ed. Pearson, 2002.

[8] M. C. Dalconi, M. Favero, G. Artioli, and U. Padova, “In-situ XRPD of hydrating cement with lab instrument : reflection vs . transmission measurements,” vol. 1, no. March 2016, pp. 155–161, 2011.

[9] M. Suryanarayana, C., Grant Norton, *X-Ray Diffraction A practical Approach*, vol. 53. 1998.

[10] R. Jenkins and R. Snyder, “Introduction to X-ray powder diffractometry,” *Intorduction to X-ray Powder Diffractometry*, pp. 47–48, 2012.

[11] Rigaku, “Differences in resolution due to differences in Soller slits,” 2015. [Online]. Available: http://www.rigaku.com/en/products/xrd/miniflex/app/1051. [Accessed: 20-Mar-2016].

[12] P. S. Eric J. Mittemeijer, *Diffraction Analysis of the Microstructure of Materials*. 2004.

[13] S. W. Smith, “Special Imaging Techniques,” *Sci. Eng. Guid. to Digit. Signal Process.*, pp. 423–450, 1997.

[14] R. C. Gonzalez and R. E. Woods, “Digital Image Processing Third Edition,” 2008.

[15] Anders Johan Nygren, “Filtered Back Projection.” [Online]. Available: http://www.owlnet.rice.edu/~elec539/Projects97/cult/node3.html#SECTION00021000000000000000. [Accessed: 25-Mar-2016].

[16] “The Rigaku Journal,” *Rigaku J.*, vol. 28, no. 1, pp. 29–30, 2012.

[17] J. I. Langford, R. J. Cernik, and D. Louer, “Breadth and shape of instrumental line profiles in high-resolution powder diffraction,” *J. Appl. Crystallogr.*, vol. 24, no. pt 5, pp. 913–919, 1991.

[18] “ZEISS Xradia 810 Ultra.” [Online]. Available: http://www.xradia.com/press-releases/xradia-introduces-ultraxrm-microscope-ground-breaking-3d-x-ray-imaging-for-laboratories/.

[19] C. J. Moran, A. Pierret, and A. W. Stevenson, “X-ray absorption and phase contrast imaging to study the interplay between plant roots and soil structure,” *Plant Soil*, vol. 223, no. 1997, pp. 99–115, 2000.

[20] Kenneth R. Spring; Thomas J. Fellers; Michael W. Davidson, “Introduction to Charge-Coupled

Devices (CCDs)," 2015. [Online]. Available: http://www.microscopyu.com/articles/digitalimaging/ccdintro.html.

[21] P. Scherrer, "Bestimmung der Grösse und der inneren Struktur von Kolloidteilchen mittels Röntgenstrahlen," *Göttingen*, vol. 2, pp. 98–100.

[22] A. R. Stokes and A. J. C. Wilson, "The diffraction of X rays by distorted crystal aggregates - I," *Proc. Phys. Soc.*, vol. 56, no. 3, pp. 174–181, 1944.

[23] G. . Williamson and W. . Hall, "X-ray Line Broadening from Filed Aluminium and Wolfram," *Acta Metall.*, vol. 1, no. 1, pp. 22–31, 1953.

[24] National Institute of Health, "ImageJ- Imaging Processing and Analysis in Java." [Online]. Available: https://imagej.nih.gov/ij/. [Accessed: 20-Mar-2016].

[25] A. L. and E. J. Mittemeijer, "Anisotrpic Strain-like Line Broadening due to Composition Variations," *Adv. X-ray Anal.*, vol. 46, p. 43, 2003.

[26] T. Ungár, "DISLOCATION MODEL OF STRAIN ANISOTROPY," *Int. Cent. Diffr. Data*, vol. 51, no. 11, pp. 76–87, 2008.

[27] A. Bazzoni, M. Cantoni, and K. L. Scrivener, "Impact of annealing on the early hydration of tricalcium silicate," *J. Am. Ceram. Soc.*, vol. 97, no. 2, pp. 584–591, 2014.

[28] M. M. C. Fernandez, "Effect of Particle Size on the Hydration Kinetics and Microstructural Development of Tricalcium Silicate," ÉCOLE POLYTECHNIQUE FÉDÉRALE DE LAUSANNE, 2008.

[29] V. Mote, Y. Purushotham, and B. Dole, "Williamson-Hall analysis in estimation of lattice strain in nanometer-sized ZnO particles," *J. Theor. Appl. Phys.*, vol. 6, no. 1, p. 6, 2012.

Appendix

Williamson-Hall plots

Small grains: For this study 32.2, 32.6, 34.2, 41.3 peaks were used.

Shown below are all points plotted (for the small grains) to illustrate non-linearity of the broadening.

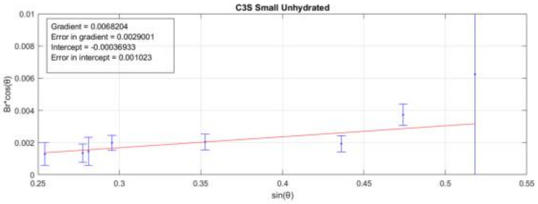

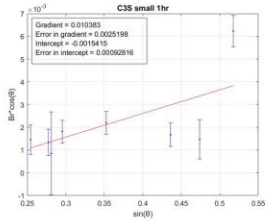

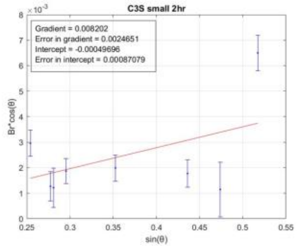

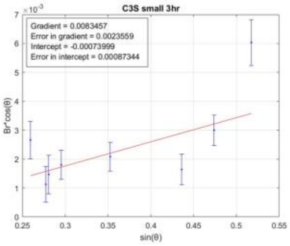

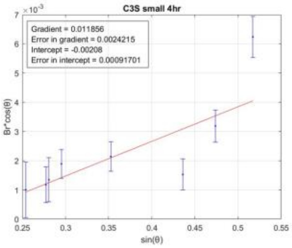

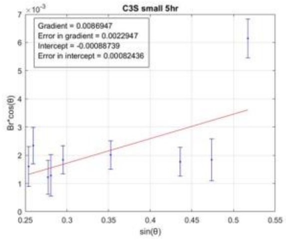

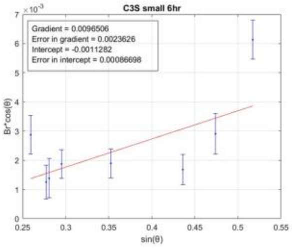

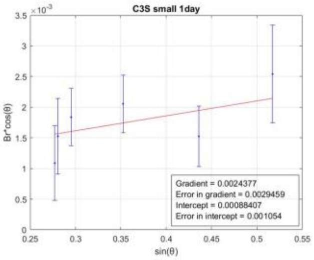

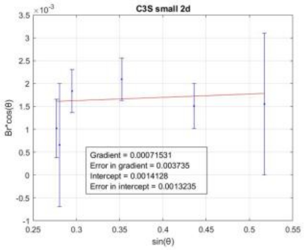

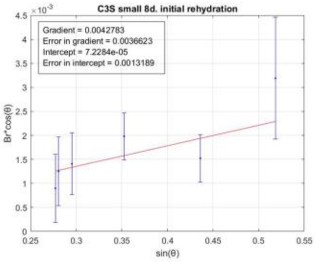

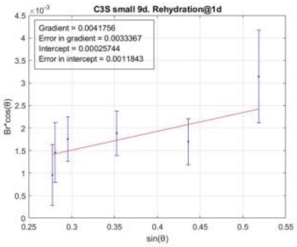

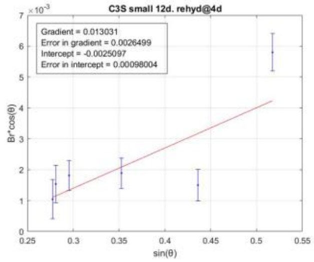

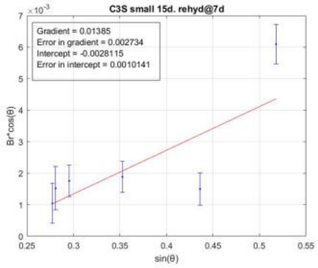

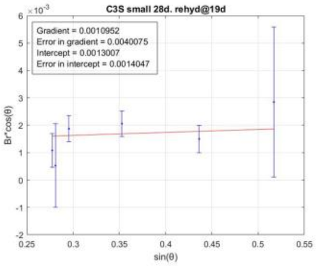

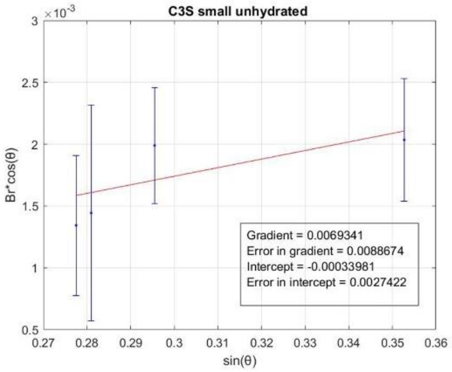
C3S small unhydrated
×10⁻³
Br*cos(θ)
sin(θ)
Gradient = 0.0069341
Error in gradient = 0.0088674
Intercept = -0.00033981
Error in intercept = 0.0027422

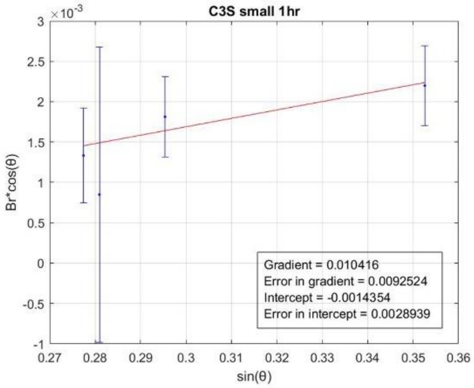
C3S small 1hr
×10⁻³
Br*cos(θ)
sin(θ)
Gradient = 0.010416
Error in gradient = 0.0092524
Intercept = -0.0014354
Error in intercept = 0.0028939

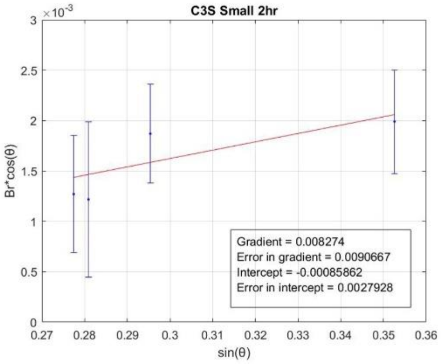
C3S Small 2hr
×10⁻³
Br*cos(θ)
sin(θ)
Gradient = 0.008274
Error in gradient = 0.0090667
Intercept = -0.00085862
Error in intercept = 0.0027928

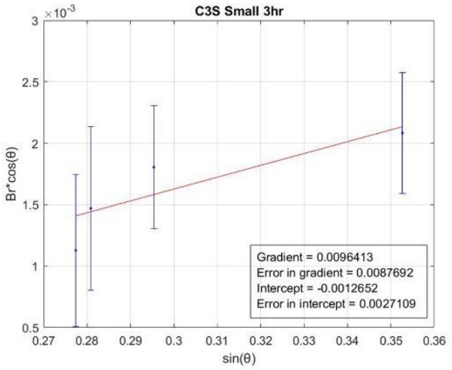
C3S Small 3hr
×10⁻³
Br*cos(θ)
sin(θ)
Gradient = 0.0096413
Error in gradient = 0.0087692
Intercept = -0.0012652
Error in intercept = 0.0027109

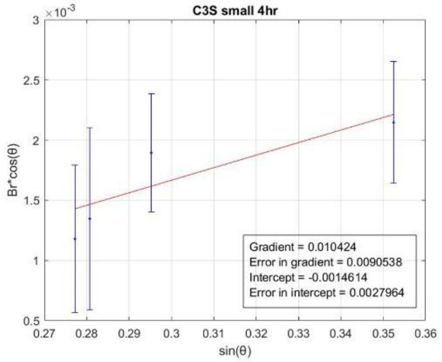
C3S small 4hr
×10⁻³
Br*cos(θ)
sin(θ)
Gradient = 0.010424
Error in gradient = 0.0090538
Intercept = -0.0014614
Error in intercept = 0.0027964

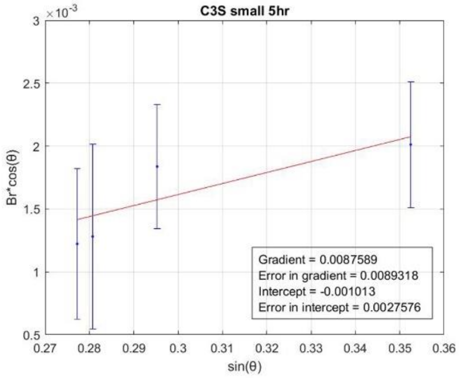
C3S small 5hr
×10⁻³
Br*cos(θ)
sin(θ)
Gradient = 0.0087589
Error in gradient = 0.0089318
Intercept = -0.001013
Error in intercept = 0.0027576

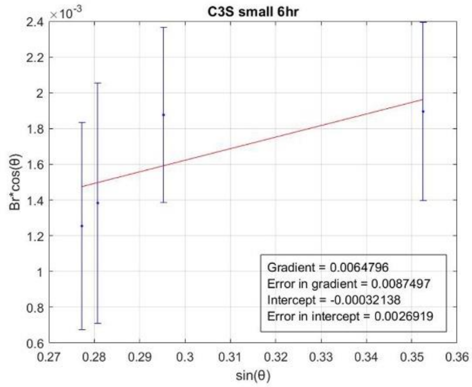
C3S small 6hr
×10⁻³
Br*cos(θ)
sin(θ)
Gradient = 0.0064796
Error in gradient = 0.0087497
Intercept = -0.00032138
Error in intercept = 0.0026919

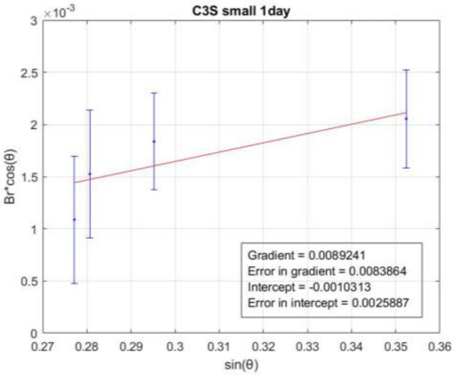
C3S small 1day
×10⁻³
Br*cos(θ)
sin(θ)
Gradient = 0.0089241
Error in gradient = 0.0083864
Intercept = -0.0010313
Error in intercept = 0.0025887

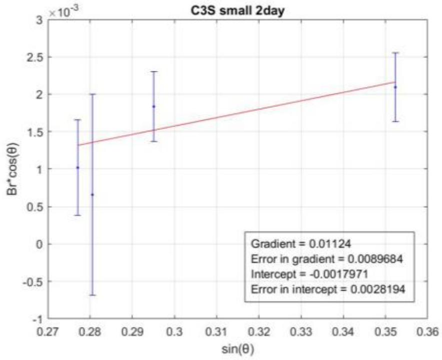
C3S small 2day
×10⁻³
Br*cos(θ)
sin(θ)
Gradient = 0.01124
Error in gradient = 0.0089684
Intercept = -0.0017971
Error in intercept = 0.0028194

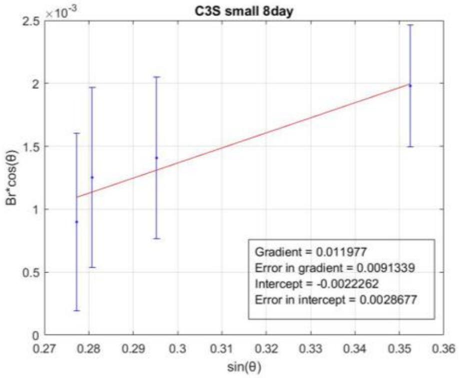
C3S small 8day
×10⁻³
Br*cos(θ)
sin(θ)
Gradient = 0.011977
Error in gradient = 0.0091339
Intercept = -0.0022262
Error in intercept = 0.0028677

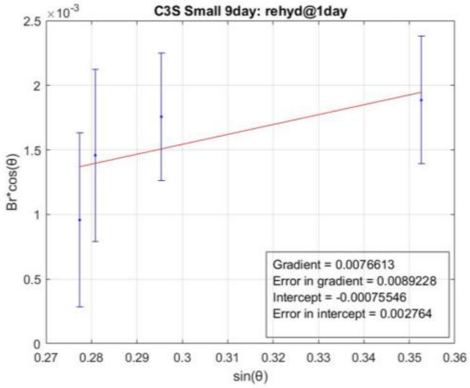
C3S Small 9day: rehyd@1day
×10⁻³
Br*cos(θ)
sin(θ)
Gradient = 0.0076613
Error in gradient = 0.0089228
Intercept = -0.00075546
Error in intercept = 0.002764

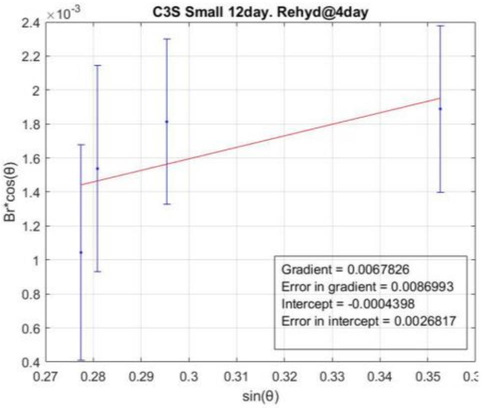
C3S Small 12day. Rehyd@4day
×10⁻³
Br*cos(θ)
sin(θ)
Gradient = 0.0067826
Error in gradient = 0.0086993
Intercept = -0.0004398
Error in intercept = 0.0026817

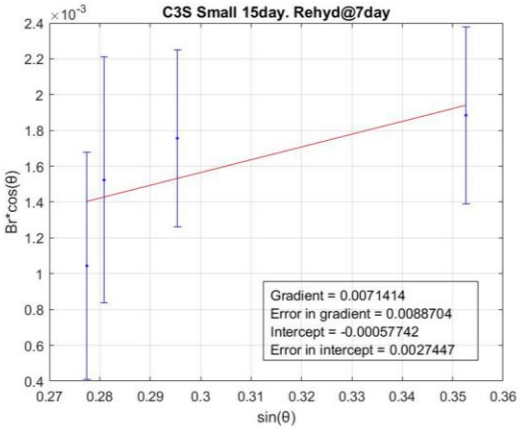
C3S Small 15day. Rehyd@7day
×10⁻³
Br*cos(θ)
sin(θ)
Gradient = 0.0071414
Error in gradient = 0.0088704
Intercept = -0.00057742
Error in intercept = 0.0027447

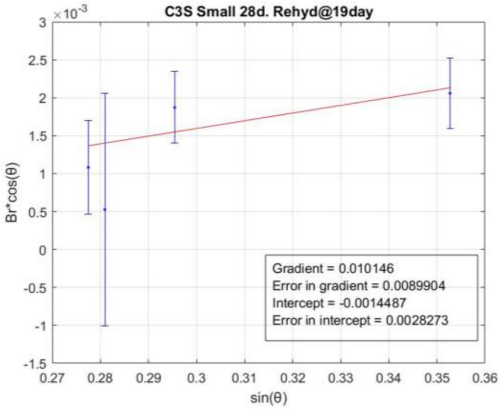
C3S Small 28d. Rehyd@19day
×10⁻³
Br*cos(θ)
sin(θ)
Gradient = 0.010146
Error in gradient = 0.0089904
Intercept = -0.0014487
Error in intercept = 0.0028273

WH plot big grains:

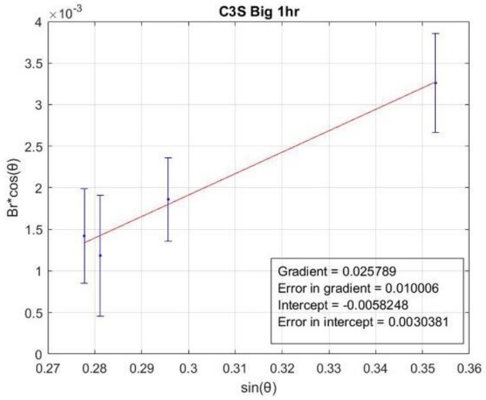

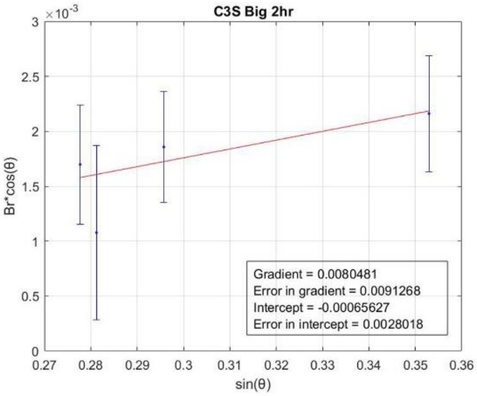

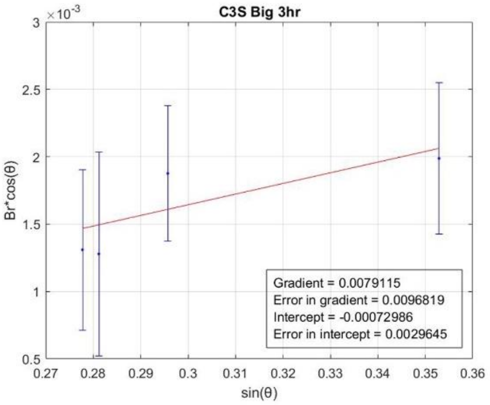

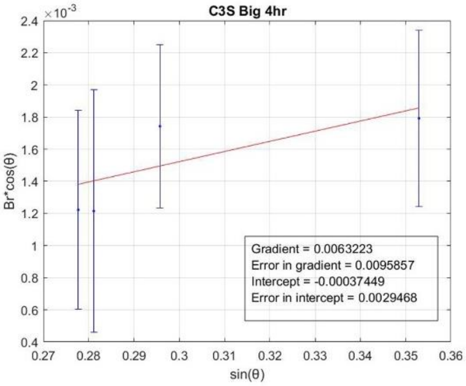

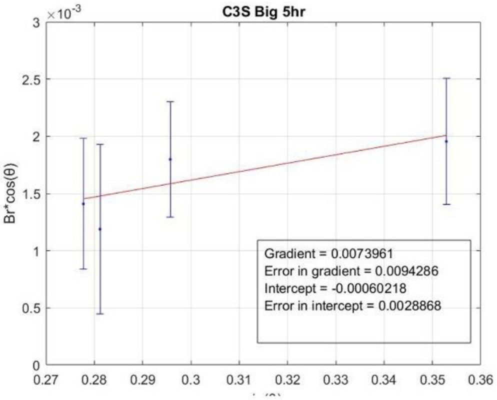

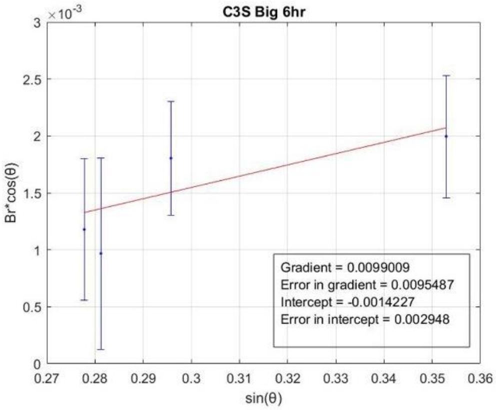

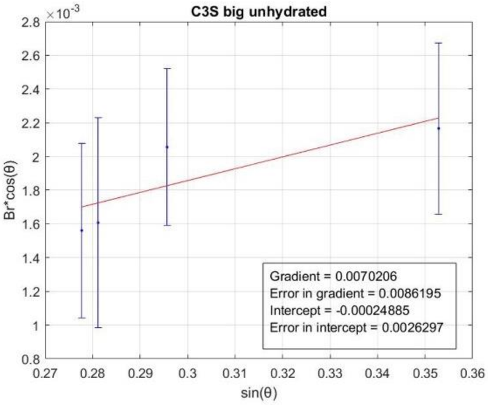

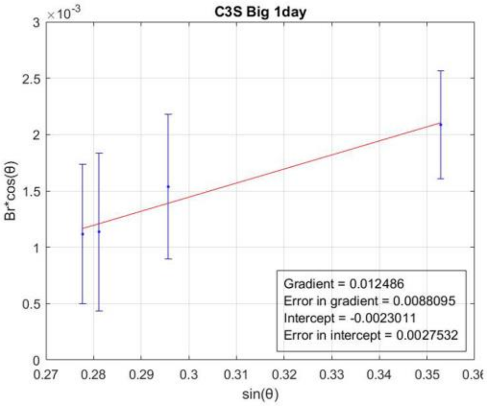
C3S Big 1day
×10^-3
3
2.5
2
1.5
1
0.5
0
Br*cos(θ)
0.27
0.28
0.29
0.3
0.31
0.32
0.33
0.34
0.35
0.3
sin(θ)
Gradient = 0.012486
Error in gradient = 0.0088095
Intercept = -0.0023011
Error in intercept = 0.0027532

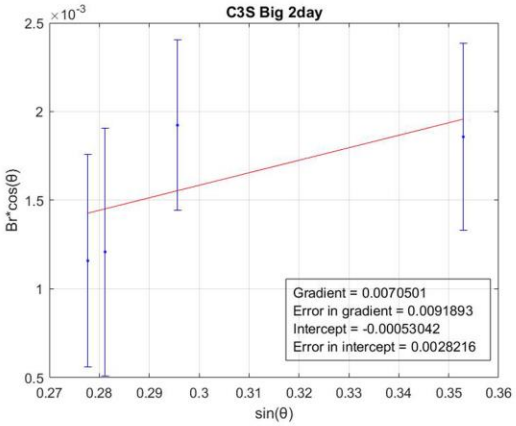
C3S Big 2day
×10^-3
2.5
2
1.5
1
0.5
Br*cos(θ)
0.27
0.28
0.29
0.3
0.31
0.32
0.33
0.34
0.35
0.36
sin(θ)
Gradient = 0.0070501
Error in gradient = 0.0091893
Intercept = -0.00053042
Error in intercept = 0.0028216

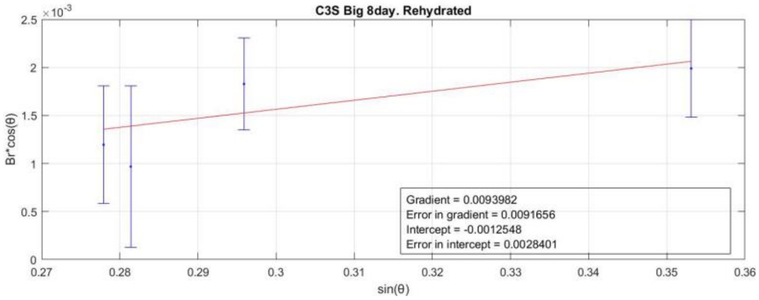
C3S Big 8day. Rehydrated
×10^-3
2.5
2
1.5
1
0.5
0
Br*cos(θ)
0.27
0.28
0.29
0.3
0.31
0.32
0.33
0.34
0.35
0.36
sin(θ)
Gradient = 0.0093982
Error in gradient = 0.0091656
Intercept = -0.0012548
Error in intercept = 0.0028401

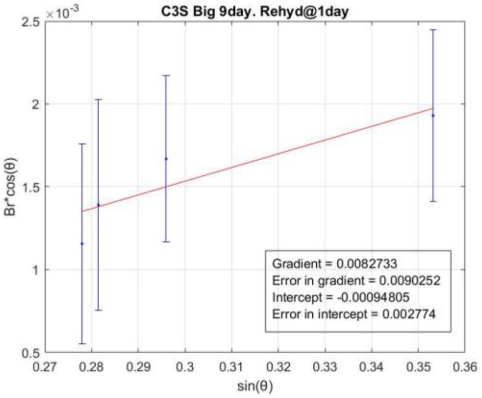
C3S Big 9day. Rehyd@1day
×10^-3
2.5
2
1.5
1
0.5
Br*cos(θ)
0.27
0.28
0.29
0.3
0.31
0.32
0.33
0.34
0.35
0.36
sin(θ)
Gradient = 0.0082733
Error in gradient = 0.0090252
Intercept = -0.00094805
Error in intercept = 0.002774

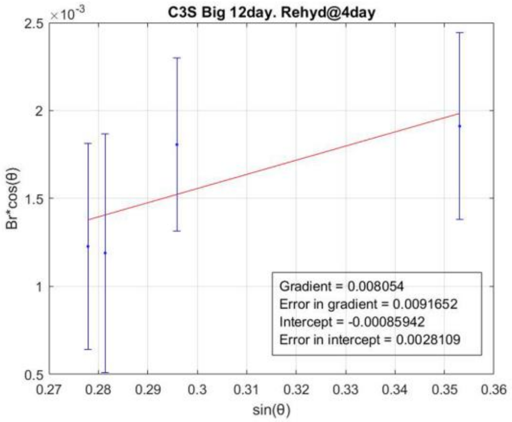
C3S Big 12day. Rehyd@4day
×10^-3
2.5
2
1.5
1
0.5
Br*cos(θ)
0.27
0.28
0.29
0.3
0.31
0.32
0.33
0.34
0.35
0.36
sin(θ)
Gradient = 0.008054
Error in gradient = 0.0091652
Intercept = -0.00085942
Error in intercept = 0.0028109

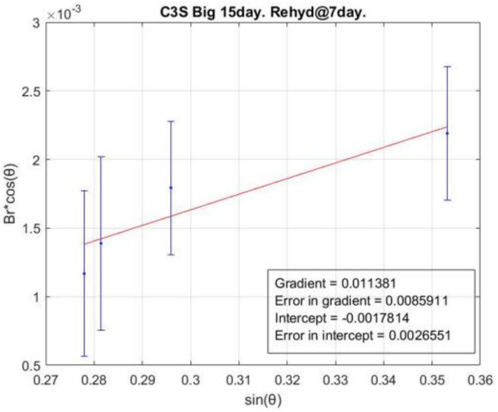
C3S Big 15day. Rehyd@7day.
×10^-3
3
2.5
2
1.5
1
0.5
Br*cos(θ)
0.27
0.28
0.29
0.3
0.31
0.32
0.33
0.34
0.35
0.36
sin(θ)
Gradient = 0.011381
Error in gradient = 0.0085911
Intercept = -0.0017814
Error in intercept = 0.0026551

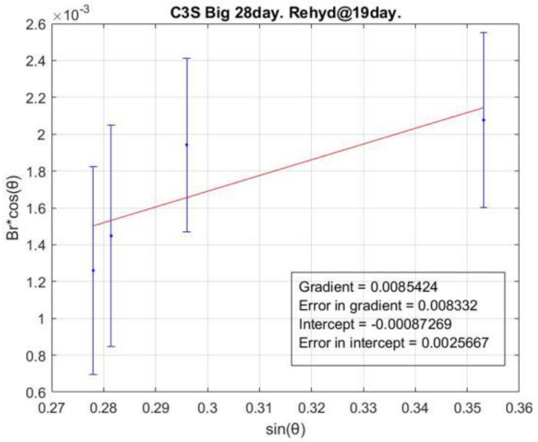
C3S Big 28day. Rehyd@19day.
×10^-3
2.6
2.4
2.2
2
1.8
1.6
1.4
1.2
1
0.8
0.6
Br*cos(θ)
0.27
0.28
0.29
0.3
0.31
0.32
0.33
0.34
0.35
0.36
sin(θ)
Gradient = 0.0085424
Error in gradient = 0.008332
Intercept = -0.00087269
Error in intercept = 0.0025667

Uncertainty Propagations

Uncertainties in the WH plots calculated using the variance formula.

$$\Delta(\beta_r \cos\theta) = \sqrt{\left(\frac{\partial z}{\partial \beta_r}\right)^2 (\Delta\beta_r)^2 + \left(\frac{\partial z}{\partial \cos\theta}\right)^2 (\Delta \cos\theta)^2}$$

Where $z = \beta_r \cos\theta$.

$\Delta\beta_r$=> ${\beta_r}^2 = {\beta_o}^2 - {\beta_i}^2 = X$, therefore $\beta_r = X^{1/2}$.

Required parameters tabulated.

$\frac{\partial z}{\partial \beta_r}$	$\frac{\partial z}{\partial \cos\theta}$	$\Delta \cos\theta$	$\Delta\beta_r$	ΔX	$\Delta{\beta_o}^2$	$\Delta{\beta_i}^2$
$\boldsymbol{\cos\theta}$	$\boldsymbol{\Delta\beta_r}$	$\boldsymbol{\sin\theta\Delta\theta}$	$\boldsymbol{\frac{\beta_r \Delta X}{2X}}$	$\sqrt{(\Delta\boldsymbol{\beta_o}^2)^2 + (\Delta\boldsymbol{\beta_i}^2)^2}$	$\boldsymbol{2\beta_p\Delta\beta_o}$	$\boldsymbol{2\beta_i\Delta\beta_i}$

Estimated standard deviations (ESD) are provided by PDXL.

ESD 2θ(rad)	$\boldsymbol{\Delta\beta_o(rad)}$	**Δ2θ(rad)**	**ESD Int W(rad)**	**Dcosθ/R**

$\Delta\beta_o = ESD(Int.W) + specimen\ shift$

Specimen shift = $\frac{D\cos\theta}{R}$; D is the specimen shift away from the reference height ~0.1mm. R= radius of goniometer (300mm for Rigaku Smartlab). Due to

$\Delta 2\theta = \Delta\theta = |2\theta_{theory} - 2\theta_{experiment}| + ESD(2\theta)$

2θ(deg)	**Int. W(deg)**	**Δint. W (deg)**	**Δbi(rad)**
28.43955	0.0935	0.002083763	2.54435E-05
47.2988	0.09035	0.001150586	
56.11833	0.0934	0.001139076	

theory 2θ (deg)	**Abs(Theory-exp)**
28.441	0.00145
47.3	0.0012
56.12	0.001675
69.126	0.001675
76.372	0.00185
88.025	0.0059
Δ2θ	0.001442

Six sets of silicon reference powder measurements were averages. The 3 most intense peaks tabulated above are used to calculate the uncertainty Δbi which is the average of the Δint. W above.